Sites of Anesthetic Inhibitory Action on a Cationic Ligand-Gated Ion Channel

Benoist Laurent, Samuel Murail, Azadeh Shahsavar, Ludovic Sauguet, Marc Delarue, Marc Baaden

Sites of Anesthetic Inhibitory Action on a Cationic Ligand-Gated Ion Channel

Benoist Laurent ‡, Samuel Murail ‡, Azadeh Shahsavar §,†, Ludovic Sauguet §,&, Marc Delarue §, &, *, Marc Baaden *

‡Laboratoire de Biochimie Théorique, CNRS, UPR9080, Univ. Paris Diderot, Sorbonne Paris Cité, 13 rue Pierre et Marie Curie, 75005 Paris, France. § Unité de Dynamique Structurale des Macromolécules, Institut Pasteur, F-75015 Paris, France & UMR 3258, Centre National de la Recherche Scientifique, F-75015 Paris, France.

Contact

* Co-corresponding authors E-mail: baaden@smplinux.de; marc.delarue@pasteur.fr.

Present Addresses

† Department of Drug Design and Pharmacology, Faculty of Health and Medical Sciences, University of Copenhagen, DK-2100 Copenhagen, Denmark.

SUMMARY: Pentameric ligand-gated ion channels have been identified as the principal target of General Anesthetics (GA), whose molecular mechanism of action remains poorly understood. Bacterial homologues, such as the *Gloeobacter violaceus* receptor (GLIC), have been shown to be valid functional models of GA action. The GA bromoform inhibits GLIC at submillimolar concentration. We characterize bromoform binding by crystallography and molecular dynamics (MD) simulations. GLIC's open form structure identified three intra-subunit binding sites. We crystallized the locally-closed form with an additional bromoform molecule in the channel pore. We systematically compare binding to the multiple potential sites of allosteric channel regulation in the open, locally-closed and resting forms. MD simulations reveal differential *exchange pathways* between sites from one form to the other. GA predominantly access the receptor from the lipid bilayer in all cases. *Differential binding affinity* among the channel forms is observed: the pore site markedly stabilizes the inactive *vs.* active state.

Introduction

Neurotransmitters and their receptors mediate fast signal transmission in the central and peripheral nervous systems. Pentameric ligand-gated ion channels (pLGICs) play a major role in this process and are among the targets of general anesthetics (Franks and Lieb, 1994). This large family of receptors can be divided in cation-selective channels such as the muscle-type nicotinic acetylcholine receptor (nAChR) with excitatory action and anion-selective channels such as the gamma-aminobutyric acid receptor ($GABA_AR$) with an inhibitory effect on neurotransmission (Corringer et al., 2012). General anesthetics (GA) at clinical concentrations act differently on both classes of receptors (Forman and Miller, 2011): they enhance inhibitory receptors (Hales and Lambert, 1991; Harrison et al., 1993; Study and Barker, 1981) and inhibit excitatory ones (Flood et al., 1997; Raines et al., 1995). These transmembrane receptors contain a pentameric subunit arrangement, with subunits divided into an extracellular (ECD) domain, a transmembrane domain (TMD), and, only in eukaryotes, an intracellular domain (Fig. 1A). The binding of neurotransmitters to the ECD allosterically triggers the opening transition in the TMD.

Electrophysiology and photo-labeling studies identified a potentiating GA binding site at subunit interfaces in the TMD, referred to as inter-subunit (IS) cavity (Mihic et al., 1997). Affinity-labelling studies of the $GABA_A$ receptor provided more detail on this IS cavity (Jayakar et al., 2014; Yip et al., 2013), corroborated by the crystal structure of the receptor presenting a large cavity precisely at the IS location (Miller and Aricescu, 2014). A structural interpretation on propofol binding followed (Franks, 2015), substantiated by a mutational study (Eaton et al., 2015). The recent cryo-microscopy structures of zebrafish GlyR show that ivermectin may come close to this cavity as well (Du et al., 2015).

In cationic ion channels, the situation is far less clear. Several additional locations with inhibitory function have been identified within the TMD subunit (Chiara et al., 2003), in the pore (Dilger et al., 1992; Nirthanan et al., 2008) and in the ECD (Chiara et al., 2003). Until recently, the lack of high-resolution structures impeded a detailed molecular interpretation of these observations, human pLGICs being notoriously difficult to crystallize. Turning to prokaryotic homologues lead to the determination of the structures from *Erwinia chrysanthemi* ELIC (Hilf and Dutzler, 2008) and from *Gloeobac-*

ter violaceus GLIC (Bocquet et al., 2009; Hilf and Dutzler, 2009; Prevost et al., 2012; Sauguet et al., 2014), paving the way for structural and mechanistic investigations. These bacterial homologs are expected to be very similar to human forms in terms of structure and pharmacology (Corringer et al., 2012; Sauguet et al., 2013a), making them a model of choice to investigate GA action. Indeed, submillimolar concentrations of bromoform inhibit wild-type GLIC (Sauguet et al., 2013a), as do other GAs, in a way similar to that of heteromeric nAchRs (Weng et al., 2010). More generally, it was shown that mechanistic aspects such as desensitization are conserved between pLGICs of prokaryotic and eukaryotic origin (Velisetty and Chakrapani, 2012). GLIC is an attractive and unique model system to decipher the molecular mechanism of GA as it has been crystallized in open (Bocquet et al., 2009; Hilf and Dutzler, 2009), locally-closed (Prevost et al., 2012) and the resting states (Sauguet et al., 2014). The locally-closed form matches the description of a postulated intermediate between the resting and active forms, namely an agonist-bound but inactive form, sometimes called a pre-activation form (Gielen et al., 2015). We need to appreciate how binding to a given receptor modifies the allosteric equilibrium between the resting (closed), active (open) and desensitized states. This objective requires structural and dynamical data missing until now, such as a description of GA binding to the different conformational states of the same receptor. Previously available structural data comprises several crystal structures of the bacterial pLGICs co-crystallized with GAs such as propofol, desflurane, ketamine and bromoform (Nury et al., 2011; Pan et al., 2012; Sauguet et al., 2013a; Spurny et al., 2013).The first structures of bacterial pLGIC showed GAs desflurane and propofol to bind to the open channel state in the TMD, to an intrasubunit site that we call DP close to the pore-lining M2 helices (Fig. 1B)(Nury et al., 2011). Bromoform adopted three distinct poses within the same cavity (Sauguet et al., 2013a): the first two are membrane-exposed and will be collectively referred to as DP-exp (the original DP site and the partially overlapping site DP' that lies closer to the M1 helix) while the third one is inserted deeper in the cavity (DP-deep), between the M1 and M2 helices (Fig. 1B). The DP site has been validated by affinity labeling techniques (Chiara et al., 2014). Based on accessibility of the residues bordering the DP site to cysteine-specific probes, Ghosh *et al.* (Ghosh et al., 2013) showed that the corresponding cavity is modified by GA binding and that the resting state of GLIC does not bind GAs in the DP site, consistent with the observation that the DP site is remodeled in the resting state crystal structure of GLIC (Sauguet et al., 2014). The pore of the ion channel is another region linked to inhibition that is likely to bind anesthetic molecules. Channel blockers are known to bind there as documented by bromo-lidocaine observed in GLIC's pore in a 3.50 Å resolution crystal structure (Hilf et al., 2010). Bromoform binding to the pore site was shown for the ELIC channel, as well as in two other sites: the inter-subunit region and the ECD (Spurny et al., 2013). A table summarizing crystal structures of GA bound to GLIC is provided as Table S1. How these structurally identified binding sites contribute to receptor inhibition remains an open question.

In addition to structural investigations, molecular dynamics (MD) simulations provide dynamic molecular-level details of GA binding to pLGICs. Using free energy calculations, the dual modulation for GLIC wild-type (inhibition) *vs.* a mutated variant (potentiation) was quantified (Bromstrup et al., 2013). Inhibition was attributed to the native DP intra-subunit site. It has since been shown that the DP site features several binding poses and additional sites have been attributed to inhibition as well. Using MD simulations, Nury *et al.* proposed a propofol binding site between subunits (Nury et al., 2011), described as "linking tunnel" connecting site DP-deep from a given subunit to an inter-subunit cavity formed with the adjacent subunit. We will call this site DP-tunnel (Fig. 1B). Mowrey *et al.* (Mowrey et al., 2013) proposed that asymmetric binding in the intra-subunit pocket would facilitate the gating transition to the resting state of GLIC, contrary to the symmetric binding to all five subunits. Brannigan *et al.* (Brannigan et al., 2010) proposed a multi-site model for isoflurane binding, with a particular interest for a pore binding site, based on simulations in an over-saturated anesthetic solution. Such simulations, here referred to as "flooding", enhance the sampling of accessible binding sites and poses. A subsequent study (LeBard et al., 2012) used free energy perturbation calculations to predict binding affinity in the pore, and hypothesized that propofol may act as pore blocker on GLIC. Willenbring *et al.* scanned GLIC for isoflurane binding sites and assessed how binding affects the structure and dynamics of the channel (Willenbring et al., 2011). A comparison of GLIC wild-type with a quadruple mutant suggested that tuning the pore-lining M2 helix tilt renders the channel insensitive to propofol (Chen et al., 2010a).

Whereas experimental and computational investigations seem to converge on the role of the potentiating IS binding site in anionic channels, the molecular mechanism of inhibition by GAs in cationic channels remains an open and controversial question. Studies on GLIC were for a long time hampered by the absence of crystals of other receptor states than the active one. Some studies hypothesized about the resting state based on available inactive structures such as ELIC, presumably in a desensitized form, yet we now know that the actual resting state structure of GLIC is quite different. The present work extends the structural and dynamic data on GA binding to multiple sites within multiple forms of the GLIC channel, including inactive ones. We systematically compare bromoform binding to multiple potential sites of allosteric channel regulation in the open, locally-closed and resting forms of GLIC. We describe by crystallography the binding of bromoform to the locally-closed structural form. An additional bromoform molecule is located in the channel pore. Flooding MD simulations reveal a new extracellular binding site only seen in the resting form, and show differen-

tial exchange pathways between sites from one form to the other. Calculated binding energies indicate significant differential affinity among the channel forms: for open *vs.* resting forms, the pore site markedly stabilizes the inactive state. The previously described intra-subunit sites mark out an entry point for GA, predominantly accessing the receptor from the lipid bilayer.

Results

Bromoform-bound crystal structures of the GLIC channel in the LC conformation reveal a new pore binding site

Bromoform contains three bromine atoms producing a specific anomalous signal that we use here to unambiguously localize these atoms in the electron density. In order to study the properties of bromoform-binding to the LC conformation of GLIC, we grew crystals of the GLIC K33C-L246C mutant (2-22', the prime numbering starts at the N-terminal end of helix M2) and K33C-N245C mutant (2-21') in presence of bromoform. These GLIC variants are particularly adapted models for this study as they both crystallize in the locally-closed conformation and 2-22' has the same electrophysiological properties as wild-type GLIC (Prevost et al., 2012). Furthermore, the transmembrane conformations in GLIC LC and in its resting state are nearly identical, with a root mean square deviation of 0.80 Å (calculated on the TMD backbone atoms and ignoring the variable M2-M3 loop). The GLIC LC conformation is believed to be a late intermediate between GLIC resting and active states and we will consider it as the best currently available model system for the TMD of the resting state, as experimental limitations preclude direct crystallization of the latter with a volatile anesthetic. Bromoform would inevitably evaporate from the mother liquor as the protocol of dehydration of the resting form crystals obtained at neutral pH, necessary to obtain medium-resolution diffraction data, requires to leave the mother liquor containing the crystals in the open air for 15-30 min. The main differences between resting and LC state are located on the upper part of the TMD and at the ECD-TMD interface as can be seen in Suppl. Fig. S1. With respect to GA binding cavities, the LC state therefore represents a good model of the TMD of the resting state, although the residues shaping the cavities might differ slightly towards the ECD-TMD interface.

The bromoform-bound structures of 2-21' and 2-22' GLIC were determined at 2.95 Å and 3.15 Å resolution, respectively (Table 1). These structures were completely superimposable with the corresponding *apo*-forms with a root mean square deviation of 0.77 Å and 0.27 Å over the 1,555 C α atoms for the 2-21' and 2-22' GLIC mutants, respectively. In the pore, we see a bromoform-binding site that is indicated by a strong Fo-Fc electron density peak (7.0 σ in 2-22', 3.9 σ in 2-21') that overlaps with a bromine-specific anomalous peak (10.0 σ in 2-22', 6.5 σ in 2-21') (Fig. 2A-B). Bromoform binds in the middle part of the pore between the Ile 240 (I9') and Ser 236 (S6') rings of residues (Fig. 2C), that are respectively involved in gating and ion permeation (Sauguet et al., 2013b). This bromoform-binding site in the ion pore of GLIC is novel and is specifically occupied when the channel is closed. In contrast, when the channel pore is open, this location is filled by ordered pentagon water molecules that were found to be critical for ion permeation (Sauguet et al., 2013b). Interestingly, bromoform was found to occupy a similar location in ELIC's closed pore (Spurny et al., 2013).

A previous study revealed that bromoform occupies alternatively three poses in the intrasubunit cavity of the GLIC open-channel structure, the double-site DP-exp, and DP-deep (Fig. 2D) (Sauguet et al., 2013a). In contrast, this intrasubunit cavity is remodelled in the GLIC locally-closed structure, thus affecting the previously described bromoform binding sites (Fig. 2D & Fig. 3). Despite the presence of an intrasubunit bromine anomalous signal in four out of five subunits in the 2-21' complex, the absence of interpretable Fo-Fc difference electron density in this location indicates either a low occupancy or a high mobility of bromoform that prevents confident model building in this DP-exp cavity. Due to the M2-M3 loop conformation that partly occludes the intrasubunit cavity, the absence of bromoform-binding at position DP-deep was *a priori* expected. In addition, bromoform-binding to the intrasubunit cavity appears to be prevented by the sidechain of residue Y197 that adopts two alternative conformations, one of which (not observed in the GLIC open crystal structure) would induce a steric clash at the DP-exp sites (Fig. 3). Finally, a phospholipid located next to DP-exp is present in GLIC open form but absent in GLIC LC. This lipid delimits the entry of the intra-subunit cavity in the open form and might favor GA-binding through van der Waals interactions. The loss of this lipid might contribute to discourage bromoform-binding to DP-exp. In summary, bromoform binding-sites are different in the LC versus the open GLIC structures: while a novel site is observed in the pore, binding to the intrasubunit cavity is discouraged in the locally-closed form.

Molecular Dynamics simulations to explore and quantify anesthetics binding

In order to characterize bromoform binding dynamics for the sites revealed by the crystallographic studies we combine three complementary simulation strategies in a fully hydrated membrane environment, summarized in Table 2. Firstly, we used flooding MD simulations of membrane-inserted GLIC in an over-saturated bromoform solution to assess the spontaneous exploration by the anesthetic and identify preferential bromoform binding sites. Three forms of GLIC were used: open, LC and resting conformations. Secondly, we ran ten 8-ns simulations of the LC form starting

with bromoform in the pore site PS to enhance sampling for this specific binding pose observed in the crystal structures. Thirdly, we determined the affinity for each binding site in open, LC and resting states using alchemical free energy calculations to quantify and compare their possible role in the inhibition process.

All TMD sites are spontaneously reachable

In the open form the flooding experiments reveal that all binding sites (i.e. DP-exp, DP-deep and PS), are spontaneously reachable in at least one of the three simulations. The observed occupancies for the DP-exp subsites DP and DP' are comparable as was observed in the crystal (respectively 0.56 and 0.43, Table 3). These occupancies are significantly higher than for site DP-deep, which agrees with the lower occupation and anomalous signal previously observed crystallographically (Sauguet et al., 2013a). In the LC conformation, site DP-deep occupancy was lower by one order-of-magnitude compared to the simulation starting from the open form. DP-deep occupancy was only observed in one subunit and displayed a particularly low residence time (3.4 ns on average). In the resting state the backbone of the upper M2 helix at the N245 position prevents occupation of the DP-deep site (Figure 4). In the flooding simulation of open GLIC the pore site PS was reached spontaneously either through the ECD vestibule or from the membrane after traversing DP-exp, -deep and -tunnel sites, whereas this access route to PS is hindered in the LC- and C-forms. The pore site is discussed in more detail in the following section. An additional binding site was observed in the lower part of the TMD, ca. 10 Å down from the DP-exp site, by simulation only. This site (called TM-down) depicted in Figure S2 is controlled by three factors, M4 helix tilt, the W213 sidechain orientation and a TM3/TM4 salt-bridge. These three factors are not simultaneously met in any available crystal structure, which may explain why the site has not been observed by crystallography so far. Overall, the DP-exp site is the most occupied one, easily reached in all functional forms of GLIC, whereas access from the membrane to the other crystallographic sites is impeded in the LC- and C-forms.

Bromoform is stable in site PS

Flooding simulations of open GLIC showed two anesthetic molecules switching from the ECD vestibule to the pore region or accessing the pore from the membrane-exposed DP-site pathway (Figure S3). The occupancy of site PS in that simulation reaches 0.50 (Tab. 3), with a total of three bromoform molecules present in the pore at the end of the simulation. One bromoform molecule was bound at the beginning of the simulation and stayed continuously in site PS for more than 400 ns before binding an upper pore site PS-up (between I9' and A13', similar to the Br-Lidocaine binding site in ELIC, PDB:2XQ3 (Hilf et al., 2010), and coming back to site PS twice for a few nanoseconds (Fig. S3A). The two other molecules were observed binding PS-up first, the first one came early (after ~100 ns) from the vestibule and stayed in the upper cavity for the rest of the simulation with the exception of one 3 ns binding event in site PS halfway through the simulation (~500 ns). The second molecule reached site PS-up from the intra subunit cavity (DP-exp for 205 ns then site DP-deep for 365 ns) at the very end of the simulation (~ 950 ns) (Fig. S3B).

In the LC and resting form simulations, anesthetics did not spontaneously reach the pore for two reasons. First, access to the vestibule was only observed once in the resting simulation and never in the LC simulation. The overall low sampling of the vestibule by bromoform is possibly due to the low concentration of solvated bromoform combined with the high polarity of the vestibule. Second, the reshaping of the intra-subunit cavity prevents an alternative access from the membrane. Ten short MD simulations of the LC state with bromoform initially bound to the pore site PS show that the anesthetic molecule remains close to this site, never leaving the region delimited by residues T226 (T2') and I233 (I9'). Hence bromoform remains stably bound at the PS site when initially placed at the crystallographic position. None of the bromoform molecules that entered the pore, subsequently left it.

In summary, MD simulations suggest that one bromoform molecule may stably occupy the pore site PS in all functional forms, and may access it either through the vestibule or through the DP-cavity from the membrane. In the open form, an additional pore site PS-up exchanging bromoform molecules with PS is observed. PS-up is able to accommodate several anesthetic molecules at the same time.

An anesthetic ECD binding cavity becomes accessible in the resting form

Bromoform binds to the ECD in a state-dependent manner as shown in Figure S4A. Three sites shown in red, cyan and dark blue are sampled with significant occupancy but do not correspond to any previously highlighted anesthetic location. In the resting form flooding experiment, a further bromoform binding site is observed: at 840 ns, a bromoform molecule enters the hydrophobic cavity detected in the apo-crystal structure of the resting state (Sauguet et al., 2014) through an opening between the bottom part of beta strand 6 (V110 to L114) and beta strand 1 (E35 to F37), reaching the so-called ES-access site in the ECD (Fig. S4). The cavity can be subdivided in two parts, a bottom part reaching up to W160, and a higher part closer to the entrance. After alternation between the two sub-cavities, bromoform moves to an upper cavity behind loop A at 960 ns, referred to here as ES site. A bromoform molecule overlapping with this site was observed crystallographically in a closed form of ELIC (Spurny et al., 2013) and a Xenon atom was also observed here in pressurized crystals of GLIC's LC-form (Sauguet *et al.*, submitted). Interestingly, in the flooding simulations, no bromoform binding to this site was observed for the open- and LC-forms, with a different ECD conformation and differ-

ent protonation state. In these forms, the R195-E32 salt-bridge prevents the opening of the beta1-beta2 loop thereby impeding access to this ECD cavity. The resting form simulation confirms the formation of a novel anesthetic pocket in the ECD for this state and shows that bromoform can spontaneously enter it.

TMD sites interconnect, with gates between them.

Considering the close vicinity of the DP-exp, DP-deep and DP-tunnel sites, we characterized the dynamics of bromoform bound to each site and examined possible paths between them. Transitions between sites and associated residence time distributions are summarized in Figure S5. Most transitions are observed in the open form, with maximal accessibilities and occupancies for all sites. Long residence times beyond the multi-nanosecond regime are observed for all sites. In the LC state, the transitions are reduced to DP-exp/DP-deep exchange and, as indicated by the residence times, resemble a flickering with short stays in DP-deep only. In the resting state, exchange is no longer observed. In all cases the broadest residence time distribution is observed for site DP-exp. It should be noted that a direct transition from the membrane to site DP-tunnel occurs for the resting state, shunting the DP–exp/DP–deep/DP–tunnel pathway as illustrated in Figure S3C.

DP-exp, an entry or waiting site to other sites.

In the flooding simulations, the membrane-exposed DP-exp site was the most occupied site. During the second half of the production run around 95 % of all bromoform molecules were located in the membrane, as a consequence the DP-exp site was the easiest to access and the first to be bound. Site DP-deep is well occupied (and hence accessible) in the open form of GLIC only. In the simulation of the LC form, the occupation of site DP-exp was close to that in the open form of GLIC, however site DP-deep was weakly occupied because the binding cavity is reshaped. In the resting form, DP-deep is not at all occupied and even within DP-exp a shift away from site DP' is observed. These changes in the LC and C forms are due to the conformations of the M2-M3 loop and of the top part of the M2 helix, preventing occupation of site DP-deep; in particular residues T244 and N245 are in close contact with this site, preventing any binding (Figure 4). A key finding is that access to the upper intersubunit DP-tunnel pocket occurs primarily through site DP-deep, itself accessed through DP-exp. From these observations we conclude that DP-site access through the membrane-exposed DP-exp cavity is controlled by the M2-M3 loop conformation imposing a barrier to reach site DP-deep in LC- and resting forms.

Y197: a gate to the inner channel.

In the crystal structures of the open and resting states, the Y197 sidechain is oriented toward the extracellular domain, with the C-Cα-Cβ-Cγ dihedral angle χ close to 167°. All available crystal structures of open and resting GLIC display Y197 residues in this "up" conformation (χ = 166 +/- 4°), while locally-closed pentamer structures of mutants 2-20', 2-22' and 2-24' display four, two and four Y197 residues in "down" conformation, respectively, characterized by χ = 60 +/- 9° with the Y197 sidechain plunging inside the intrasubunit pocket. During the MD simulations, χ oscillated between two modes at 170° and 73° (Fig. S6) with only a few transitions. Both conformations were approximately equally sampled in the LC- and open forms, whereas the "down" conformation was preferred for the resting form, even though this simulation started from an "up" conformation. Even though Y197 is not in the immediate environment of bromoform in the crystal structure, it dramatically modulates the volume of the intrasubunit pocket (Fig. 3), as proposed by Mowrey *et al.* (Mowrey et al., 2013), overlapping in particular the DP' subsite of DP-exp and preventing bromoform from entering any deeper. In summary, the slow transitions of the Y197 residue to a "down" conformation act like a gate shutting off access to DP-deep and -tunnel sites.

Bromoform binding affinities are energetically favorable for all binding sites.

Binding affinities were calculated with respect to the pure aqueous phase as reference state. As the true reference state should be taken at the water-membrane interface (Fig. S7), only relative values of $\Delta\Delta G$ are meaningful. Bromoform affinity for the binding poses observed in the crystal structures of open and locally-closed states ranges from -7.5 kcal/mol to -5.2 kcal/mol (see Fig. 5 and Table S3). In the ECD, the binding affinity for the ES site seen by simulation only is -4.9 kcal/mol, irrespective of the channel form, corroborating the idea that site accessibility and not affinity differentiates the resting form from LC and open ones. Concerning the TMD, in the open form all binding sites have comparable energies in the -5.2 to -5.8 kcal/mol range. By reshaping the cavity in the LC- and C-forms, energies are shifted. DP-exp becomes more favorable by 1.4 and 1.1 kcal/mol for LC- and C-forms, respectively. As expected from the steric hindrance induced by the M2-M3 loop, the DP-deep and DP-tunnel sites become less favorable by 1.2 to 2.9 kcal/mol. The effect is more pronounced for the LC-state, where M2-M3 interferes more strongly with possible bromoform binding and Y197 is in the down conformation adding to the site constriction. The pore sites PS and PS-up display the most favorable free energies of binding with a higher affinity in the LC- and C-forms compared to open state, exhibiting a $|\Delta\Delta G|$ between 3.2 and 0.6 kcal/mol, respectively. This set of quantified binding affinities documents that M2-M3

and Y197 conformations directly modulate binding to DP-deep and –tunnel sites. Binding to DP-exp and PS/PS-up sites is particularly strong in the LC- and C-forms.

Discussion

A picture of dynamically accessible and interconnected anesthetic binding sites in cationic pLGIC emerges from the computational investigations of our study, in good agreement with the provided crystallographic data, allowing to quantitatively describe the dynamics of transitions between sites and their binding affinities. Our study includes data on inactive channel states that were hitherto missing. Modulations of GA binding occur as a function of channel state, as we show very clearly. We confirm that the previously described GA binding site in ELIC within the channel pore is present in GLIC and show how it is connected to the other sites. We point to novel sites in the extracellular and transmembrane domains. Relating the observed GA dynamics to functional transitions of the channel requires longer simulations. The GA transitions themselves are controlled by specific gate residues that we were able to point out. The principal GA access pathway to the channel most probably originates from the membrane.

Anesthetics access multiple receptor binding sites through the membrane

Evidence that anesthetics bind the intrasubunit site in the DP-exp region is strong. Crystal structures showed that bromoform (Sauguet et al., 2013a), propofol and desflurane bind to this pocket (Chiara et al., 2014; Nury et al., 2011). The data collected in the present work clearly show that intrasubunit sites revealed by crystallographic data are spontaneously accessible in MD simulations and display favorable free energies of binding. In the simulations, access to all these GA binding sites in the TMD seems to occur from the membrane mainly through DP-exp. This observation may be explained by the fact that the membrane acts as the main reservoir of GA molecules in the system. From this common entry point anesthetics can then move to any of the other TMD sites. Some sites may occasionally be accessed directly from the membrane, shunting DP-exp, as seen once for the DP-tunnel site. For the pore site, an additional pathway from the ECD-vestibule is observed (Figure S3). Other routes cannot be excluded, especially as GA movement between sites is free, but seem unlikely in light of the marginal anesthetic concentration in the aqueous phase. On this basis, GA access from the membrane appears as a plausible hypothesis. More statistics would be required to conclude whether DP-exp is the principal GA entrance point.

Because multiple GA binding sites in the TM- and EC domains are described in the present work we may raise the question which ones trigger receptor inhibition. We observed several binding sites in the ECD and focused our attention on site ES, as an overlapping site was identified in ELIC (Spurny et al., 2013) and a close-by vestibule site, ca. 4-5 Å away, was seen on AchBP (Spurny et al., 2015). Free energy calculations revealed that no state-dependent affinity modulation - as expected for an inhibitory site - occurs for the ES location that is only sterically accessible in the resting state conformation. This finding suggests that the inhibitory site(s) cannot be ES. A novel TM-down site was observed involving the L209 and S212 residues on TM1. Equivalent positions of the $\alpha 7$ nicotinic acetylcholine receptor were previously suggested to be part of a potentiating site, their A225D and S222M mutations affecting receptor potentiation by PNU-120596 (Young et al., 2008). Hence the TM-down site is an unlikely candidate for inhibition. Concerning the channel pore, MD simulations confirm the PS binding site revealed by crystallography and further indicate a second PS-up subsite. These findings echo experimental observations on ELIC (Spurny et al., 2013) as well as previous simulations on GLIC and nAChR (Brannigan et al., 2010; LeBard et al., 2012). All cationic channels feature a hydrophobic pore providing a favorable environment for binding and inhibition by GA. Free energy calculations (Fig. 5) confirm very favorable and state-dependent binding affinities for both PS- and PS-up sites. Binding to the pore region is likely absent in anionic channels such as GABA and GlyR, potentiated by GA, as they feature a polar pore. This property is apparent in the recent structures by (Du et al., 2015), where the channel pore is lined by a series of Thr residues. These observations taken together lead to the hypothesis that GA binding to the channel pore may be part of the universal hallmark of GA inhibition specific for cationic pLGICs. A possible inhibition mechanism would involve shifting the conformational equilibrium towards the closed state by maximizing GA binding locally in the TMD pore region first, to subsequently trigger allosteric changes throughout TMD and ECD. To assess whether any such proposed mechanism may be unitary, more structural data on a broader range of molecules would be required.

An apparent contradiction in our data concerns the existence of pore binding site(s) in the open channel state, suggested by MD simulations but not observed by crystallography. In the simulations, we observe - on average and after initial relaxation - a slightly more closed pore than in the crystal environment, creating a favorable environment for GA binding. The intrinsic thermal fluctuations of the channel in the membrane environment and the absence of detergent molecules in the pore further enhance the GA affinity of this region. In the crystal, the PS-up sub-site is sterically hindered by detergent molecules. Furthermore, the open state of the channel features a wetted pore with a specific pentagonal water pattern and provides a less hydrophobic environment for pore-binding. The bromoform force field parameters might be another source of inaccuracies. These factors taken together may explain the discrepancy between

simulations and crystallographic evidence for the open-channel bromoform binding to the pore. The pore-binding data on the inactive channel states is fully consistent between simulation and experiment.

We describe the dynamic interplay between multiple GA binding sites, showing a high mobility of bromoform within these regions (see Fig. S5). We observe an important exchange rate between site DP-exp and site DP-deep over the microsecond period. Several transitions occur from site DP-deep to site DP-tunnel, an intersubunit site described in GLIC on the basis of MD simulations (Nury et al., 2011) with respectively desflurane and *ortho*-propofol diazirine. The anesthetic can reach site DP-tunnel either directly from the membrane – only observed once in all our simulations – or through a route traversing sites DP-exp and DP-deep. This route can be occluded by the Y197 residue whose sidechain orientation is critical for anesthetic binding and insertion depth. In addition, the bending of M2 helices in the locally-closed conformation moves residues from the top of M2 and from the M2-M3 loop inside the intrasubunit pocket, in particular residue T244 (Fig. 4). Free energy calculations show that site DP-exp is clearly more favorable to bromoform than site DP-deep in the LC structures, while in GLIC's open form, this difference is less marked (Fig. 5). Structural alignments reveal that Y197 is highly conserved among Cys-loop receptors, including nicotinic acetylcholine, $5HT_3$ and glycine receptors (Sauguet et al., 2013a). It is an interesting target for mutagenesis studies: less occluding sidechains should facilitate the passage of anesthetics, whereas sidechains filling the down position would impede their penetration. Y197 orientation affects the rotamer distribution of the F195 residue, which may modulate GLIC gating, given its direct interaction with the M2-M3 helix; actually a F195A mutant shows a strong loss of function phenotype (Sauguet et al., 2014). Further interesting hypotheses about mutations may be derived from the simulations, e.g. to render a specific binding site in a specific receptor state more or less favorable to enhance or prevent binding, respectively. To this purpose we will provide representative snapshots upon request.

Implications for GA-induced receptor inhibition and limitations of the study

At present, it remains a challenge to precisely link this coherent and detailed experimental and computational description of GA binding to GLIC open, LC and resting states to the anesthetic mechanism of inhibition. A key element for such an interpretation is the induced difference in GA binding affinity for several sites in the inactive states (Fig. 1). Free energy calculations showed state-dependent affinities for all tested sites except for site ES. Relatively small changes in such affinities may lie well below potential errors arising from e.g. the choice of force field, initial sidechain orientation, slow relaxation of the binding site, etc. Such intrinsic limits are discussed in more detail in the literature (Chodera et al., 2011; Hansen and van Gunsteren, 2014). From our experience, we estimate a confidence limit of ca. 1 kcal/mol, significantly higher than the observed statistical error. This estimation is in line with a recent large-scale assessment (Mikulskis et al., 2014). A marked affinity preference for the inactive *vs.* open states is observed for the upper pore site PS2, and to a lesser extent for DP-exp. Site PS features more subtle changes with a similar trend. For DP-tunnel and DP-deep, the open state is favored. Affinity data on inactive states is key to distinguish the different sites, as open state affinities alone are very similar throughout. From these results the pore region emerges as a particularly favorable location for channel inhibition by GA. Our results further illustrate that a large receptor can have a network of interconnected anesthetic binding sites. Although it is likely that only some of these sites produce functional effects, disentangling which ones are responsible for inhibition is not a fully solved issue yet.

In this work, the effect of GA binding on GLIC was investigated for three states, one activated and two inactive ones. To further improve our understanding of the inhibition mechanism, it would be interesting to extend the study to the desensitized state of GLIC. For example, some studies on nAChR previously suggested GA action on the desensitized state (Jayakar et al., 2013; Jayakar et al., 2014). At present, we lack detailed structural information on this channel state. Based on spin-label distance measurements by EPR (Velisetty and Chakrapani, 2012; Velisetty et al., 2014), the structural changes at the ECD/TMD interface have been postulated as possible target for allosteric modulators such as anesthetics. This hypothesis is in line with the observed modulation of bromoform binding pockets through conformational changes of the receptor (Figure S8). Within the context of our findings, we noted some hindrance for access to the transmembrane sites in the resting state, which might appear counter-intuitive. How this intra-subunit site is remodelled in the desensitized state would be an interesting complementary observation. We note that DEER/EPR studies revealed the existence of a "desensitization-gate" in the middle of the pore, precisely at the level of the GA pore-binding-site (Velisetty and Chakrapani, 2012).

Conclusion

Multiple potential sites of allosteric regulation by bromoform exist for the GLIC channel. Bromoform binding to the open, locally-closed (pre-activation) and resting forms revealed state-modulated affinities with two sites in the channel pore clearly stabilizing the resting state compared to the active one. Crystal structures of bromoform bound to the locally closed (pre-activation) GLIC channel, feature an additional bromoform molecule located in the pore. Access to this pore site mainly occurs from the membrane. These elements let the pore site appear as a good candidate for specific functional effects of anesthetics on cationic channels, featuring a more hydrophobic channel interior than anionic ones.

Other dynamically accessible and interconnected binding sites may still contribute to inhibition, eventually by stabilizing the desensitized channel state for which structural data is yet missing.

Experimental Procedures

Crystallography

Protein production

Each mutant of GLIC fused to maltose-binding protein was expressed in *E. coli* C43 cells and purified as described in (Bocquet et al., 2007). The resulting fusion protein was cleaved and concentrated as before.

Crystallization

All crystals were obtained using the hanging drop vapor diffusion method at 20°C. The concentrated protein (6-8 mg/ml) was mixed in a 1:1 ratio with reservoir solution containing 0.1 M NaAcetate pH 4, 0.4 M NaSCN, 12-16% PEG 4000, 17% Glycerol and 2% w/v of bromoform to obtain co-crystals. Crystallization was induced by micro-seeding technique from a solution of crushed crystals 1 hour after setting up the crystallization experiment

Data collection. Datasets were collected on beamline Proxima-1 of the Soleil Synchrotron (Gif-sur-Yvette, France) and ID23-1 of the European Synchrotron Radiation Facility (Grenoble, France). Diffraction data were collected using the inverse-beam data collection facility in order to maximize the anomalous scattering signal. Reflections were integrated using XDS (Kabsch, 2010) and further processed using the CCP4 programs (Evans, 2011; Winn et al., 2011). Details on the data collection statistics are provided in Table 1.

Phasing and refinement

The molecular replacement solution was found in Phaser (McCoy et al., 2007). The initial model was refined either in Refmac 5 (Murshudov et al., 1997) or Phenix (Afonine et al., 2012) by using rigid-body refinement and subsequently, restrained refinement (Murshudov et al., 1997). The resulting model was improved by manual building in COOT (Emsley and Cowtan, 2004). The model was finally refined in Buster (Blanc et al., 2004). B-factors were refined using 1 translation-libration-screw (TLS) parameter by chain. Five-fold non-crystallographic symmetry (NCS) averaging was used to improve the quality of the electron density thus allowing the unambiguous reconstruction of the complete model. Molprobity (Chen et al., 2010b) scores for the refined models ranged within the 100th percentiles of structures refined at comparable resolutions. Details of the refinement statistics are provided in Table 1.

Molecular dynamics simulations

Molecular dynamics simulations of open and closed GLIC were set up using PDB-ids 4HFI and 4NPQ, respectively. The locally-closed simulations were built upon the 2-22' crystal structure presented in this work. For LC and open models residue protonation states were assigned as in previous simulations (Nury et al., 2011; Prevost et al., 2012). For the closed state, protonation was assigned to mimic a pH 7.0 condition; the default protonation was used with the only exception of H127 being doubly protonated. Each model was inserted into a pre-equilibrated lipid bilayer and relaxed prior to the production phase. Simulations were performed using the CHARMM-36 all-atom force field. System composition is detailed in Tab. S3. We carried out short MD simulations where bromoform poses were generated by randomly moving and rotating molecules around the crystallographic binding site achieving a total of 125 different poses to maximize bromoform sampling in the binding pocket. For long MD simulations we used four iterations to add bromoform slowly and avoid aggregates due to its low solubility. In each iteration, 50 molecules were added by replacing random water molecules 10 Å away of protein and 4 Å away of the membrane. The equilibrated system was used as starting point for 1 μs production runs of flooding simulations. For free energy of binding energy calculations, the bromoform poses displayed in the crystal structure were used when available; in inter-subunit site B2 it was extracted from a short MD simulation. A thermodynamic cycle was applied to calculate free energies of binding of bromoform to GLIC using a similar protocol as that described in (Bromstrup et al., 2013). The calculation of the binding free energy was carried out using the Bennett acceptance ratio method (BAR)(Bennett, 1976) as implemented in the GROMACS g_bar program. Full details are available in SI methods.

SUPPLEMENTAL INFORMATION

Supplemental Experimental Procedures, eight figures and four tables can be found with this article online.

AUTHOR CONTRIBUTIONS

The manuscript was written through contributions of all authors. All authors have given approval to the final version of the manuscript. ‡These authors contributed equally.

ACKNOWLEDGMENT

The authors thank Torben Brömstrup, Pierre-Jean Corringer, Jérôme Hénin and Erik Lindahl for fruitful discussions. This work was supported by Les Laboratoires Servier, the French Agency for Research and the “Initiative d’Excellence” program (Grants ANR-11-MONU-003, ANR-2010-BLAN-1534, ANR-13-BSV8-0020, ANR-11-LABX-0011), the Fondation Pierre Gilles de Gennes, the École Doctorale Interdisciplinaire Européenne Frontières du vivant ED474 Liliane Bettencourt doctoral program, and CNRS.

REFERENCES

Afonine, P.V., Grosse-Kunstleve, R.W., Echols, N., Headd, J.J., Moriarty, N.W., Mustyakimov, M., Terwilliger, T.C., Urzhumtsev, A., Zwart, P.H., and Adams, P.D. (2012). Towards automated crystallographic structure refinement with phenix.refine. Acta crystallographica. Section D, Biological crystallography *68*, 352-367.

Bennett, C.H. (1976). Efficient estimation of free energy differences from Monte Carlo data. Journal of Computational Physics *22*, 245-268.

Blanc, E., Roversi, P., Vonrhein, C., Flensburg, C., Lea, S.M., and Bricogne, G. (2004). Refinement of severely incomplete structures with maximum likelihood in BUSTER-TNT. Acta crystallographica. Section D, Biological crystallography *60*, 2210-2221.

Bocquet, N., Nury, H., Baaden, M., Le Poupon, C., Changeux, J.P., Delarue, M., and Corringer, P.J. (2009). X-ray structure of a pentameric ligand-gated ion channel in an apparently open conformation. Nature *457*, 111-114.

Bocquet, N., Prado de Carvalho, L., Cartaud, J., Neyton, J., Le Poupon, C., Taly, A., Grutter, T., Changeux, J.P., and Corringer, P.J. (2007). A prokaryotic proton-gated ion channel from the nicotinic acetylcholine receptor family. Nature *445*, 116-119.

Brannigan, G., LeBard, D.N., Henin, J., Eckenhoff, R.G., and Klein, M.L. (2010). Multiple binding sites for the general anesthetic isoflurane identified in the nicotinic acetylcholine receptor transmembrane domain. Proceedings of the National Academy of Sciences of the United States of America *107*, 14122-14127.

Bromstrup, T., Howard, R.J., Trudell, J.R., Harris, R.A., and Lindahl, E. (2013). Inhibition versus potentiation of ligand-gated ion channels can be altered by a single mutation that moves ligands between intra- and intersubunit sites. Structure *21*, 1307-1316.

Chen, Q., Cheng, M.H., Xu, Y., and Tang, P. (2010a). Anesthetic binding in a pentameric ligand-gated ion channel: GLIC. Biophys J *99*, 1801-1809.

Chen, V.B., Arendall, W.B., 3rd, Headd, J.J., Keedy, D.A., Immormino, R.M., Kapral, G.J., Murray, L.W., Richardson, J.S., and Richardson, D.C. (2010b). MolProbity: all-atom structure validation for macromolecular crystallography. Acta crystallographica. Section D, Biological crystallography *66*, 12-21.

Chiara, D.C., Dangott, L.J., Eckenhoff, R.G., and Cohen, J.B. (2003). Identification of nicotinic acetylcholine receptor amino acids photolabeled by the volatile anesthetic halothane. Biochemistry *42*, 13457-13467.

Chiara, D.C., Gill, J.F., Chen, Q., Tillman, T., Dailey, W.P., Eckenhoff, R.G., Xu, Y., Tang, P., and Cohen, J.B. (2014). Photoaffinity labeling the propofol binding site in GLIC. Biochemistry *53*, 135-142.

Chodera, J.D., Mobley, D.L., Shirts, M.R., Dixon, R.W., Branson, K., and Pande, V.S. (2011). Alchemical free energy methods for drug discovery: progress and challenges. Current opinion in structural biology *21*, 150-160.

Corringer, P.J., Poitevin, F., Prevost, M.S., Sauguet, L., Delarue, M., and Changeux, J.P. (2012). Structure and pharmacology of pentameric receptor channels: from bacteria to brain. Structure *20*, 941-956.

Dilger, J.P., Brett, R.S., and Lesko, L.A. (1992). Effects of isoflurane on acetylcholine receptor channels. 1. Single-channel currents. Molecular pharmacology *41*, 127-133.

Du, J., Lu, W., Wu, S., Cheng, Y., and Gouaux, E. (2015). Glycine receptor mechanism elucidated by electron cryo-microscopy. Nature *526*, 224-229.

Eaton, M.M., Cao, L.Q., Chen, Z., Franks, N.P., Evers, A.S., and Akk, G. (2015). Mutational Analysis of the Putative High-Affinity Propofol Binding Site in Human beta3 Homomeric GABAA Receptors. Molecular pharmacology *88*, 736-745.

Emsley, P., and Cowtan, K. (2004). Coot: model-building tools for molecular graphics. Acta crystallographica. Section D, Biological crystallography *60*, 2126-2132.

Evans, P.R. (2011). An introduction to data reduction: space-group determination, scaling and intensity statistics. Acta crystallographica. Section D, Biological crystallography *67*, 282-292.

Flood, P., Ramirez-Latorre, J., and Role, L. (1997). Alpha 4 beta 2 neuronal nicotinic acetylcholine receptors in the central nervous system are inhibited by isoflurane and propofol, but alpha 7-type nicotinic acetylcholine receptors are unaffected. Anesthesiology *86*, 859-865.

Forman, S.A., and Miller, K.W. (2011). Anesthetic sites and allosteric mechanisms of action on Cys-loop ligand-gated ion channels. Canadian journal of anaesthesia = Journal canadien d'anesthesie *58*, 191-205.

Franks, N.P. (2015). Structural comparisons of ligand-gated ion channels in open, closed, and desensitized states identify a novel propofol-binding site on mammalian gamma-aminobutyric acid type A receptors. Anesthesiology *122*, 787-794.

Franks, N.P., and Lieb, W.R. (1994). Molecular and cellular mechanisms of general anaesthesia. Nature *367*, 607-614.

Ghosh, B., Satyshur, K.A., and Czajkowski, C. (2013). Propofol binding to the resting state of the gloeobacter violaceus ligand-gated ion channel (GLIC) induces structural changes in the inter- and intrasubunit transmembrane domain (TMD) cavities. J Biol Chem *288*, 17420-17431.

Gielen, M., Thomas, P., and Smart, T.G. (2015). The desensitization gate of inhibitory Cys-loop receptors. Nature communications *6*, 6829.

Hales, T.G., and Lambert, J.J. (1991). The actions of propofol on inhibitory amino acid receptors of bovine adrenomedullary chromaffin cells and rodent central neurones. Br J Pharmacol *104*, 619-628.

Hansen, N., and van Gunsteren, W.F. (2014). Practical Aspects of Free-Energy Calculations: A Review. Journal of chemical theory and computation *10*, 2632-2647.

Harrison, N.L., Kugler, J.L., Jones, M.V., Greenblatt, E.P., and Pritchett, D.B. (1993). Positive modulation of human gamma-aminobutyric acid type A and glycine receptors by the inhalation anesthetic isoflurane. Molecular pharmacology *44*, 628-632.
Hilf, R.J., Bertozzi, C., Zimmermann, I., Reiter, A., Trauner, D., and Dutzler, R. (2010). Structural basis of open channel block in a prokaryotic pentameric ligand-gated ion channel. Nat Struct Mol Biol *17*, 1330-1336.
Hilf, R.J., and Dutzler, R. (2008). X-ray structure of a prokaryotic pentameric ligand-gated ion channel. Nature *452*, 375-379.
Hilf, R.J., and Dutzler, R. (2009). Structure of a potentially open state of a proton-activated pentameric ligand-gated ion channel. Nature *457*, 115-118.
Jayakar, S.S., Dailey, W.P., Eckenhoff, R.G., and Cohen, J.B. (2013). Identification of propofol binding sites in a nicotinic acetylcholine receptor with a photoreactive propofol analog. J Biol Chem *288*, 6178-6189.
Jayakar, S.S., Zhou, X., Chiara, D.C., Dostalova, Z., Savechenkov, P.Y., Bruzik, K.S., Dailey, W.P., Miller, K.W., Eckenhoff, R.G., and Cohen, J.B. (2014). Multiple propofol-binding sites in a gamma-aminobutyric acid type A receptor (GABAAR) identified using a photoreactive propofol analog. J Biol Chem *289*, 27456-27468.
Kabsch, W. (2010). Xds. Acta crystallographica. Section D, Biological crystallography *66*, 125-132.
LeBard, D.N., Henin, J., Eckenhoff, R.G., Klein, M.L., and Brannigan, G. (2012). General anesthetics predicted to block the GLIC pore with micromolar affinity. PLoS Comput Biol *8*, e1002532.
McCoy, A.J., Grosse-Kunstleve, R.W., Adams, P.D., Winn, M.D., Storoni, L.C., and Read, R.J. (2007). Phaser crystallographic software. J Appl Crystallogr *40*, 658-674.
Mihic, S.J., Ye, Q., Wick, M.J., Koltchine, V.V., Krasowski, M.D., Finn, S.E., Mascia, M.P., Valenzuela, C.F., Hanson, K.K., Greenblatt, E.P.*, et al.* (1997). Sites of alcohol and volatile anaesthetic action on GABA(A) and glycine receptors. Nature *389*, 385-389.
Mikulskis, P., Genheden, S., and Ryde, U. (2014). A large-scale test of free-energy simulation estimates of protein-ligand binding affinities. Journal of chemical information and modeling *54*, 2794-2806.
Miller, P.S., and Aricescu, A.R. (2014). Crystal structure of a human GABAA receptor. Nature *512*, 270-275.
Mowrey, D., Cheng, M.H., Liu, L.T., Willenbring, D., Lu, X., Wymore, T., Xu, Y., and Tang, P. (2013). Asymmetric ligand binding facilitates conformational transitions in pentameric ligand-gated ion channels. J Am Chem Soc *135*, 2172-2180.
Murshudov, G.N., Vagin, A.A., and Dodson, E.J. (1997). Refinement of macromolecular structures by the maximum-likelihood method. Acta crystallographica. Section D, Biological crystallography *53*, 240-255.
Nirthanan, S., Garcia, G., 3rd, Chiara, D.C., Husain, S.S., and Cohen, J.B. (2008). Identification of binding sites in the nicotinic acetylcholine receptor for TDBzl-etomidate, a photoreactive positive allosteric effector. J Biol Chem *283*, 22051-22062.
Nury, H., Van Renterghem, C., Weng, Y., Tran, A., Baaden, M., Dufresne, V., Changeux, J.P., Sonner, J.M., Delarue, M., and Corringer, P.J. (2011). X-ray structures of general anaesthetics bound to a pentameric ligand-gated ion channel. Nature *469*, 428-431.
Pan, J., Chen, Q., Willenbring, D., Mowrey, D., Kong, X.P., Cohen, A., Divito, C.B., Xu, Y., and Tang, P. (2012). Structure of the pentameric ligand-gated ion channel GLIC bound with anesthetic ketamine. Structure *20*, 1463-1469.
Prevost, M.S., Sauguet, L., Nury, H., Van Renterghem, C., Huon, C., Poitevin, F., Baaden, M., Delarue, M., and Corringer, P.J. (2012). A locally closed conformation of a bacterial pentameric proton-gated ion channel. Nat Struct Mol Biol *19*, 642-649.
Raines, D.E., Rankin, S.E., and Miller, K.W. (1995). General anesthetics modify the kinetics of nicotinic acetylcholine receptor desensitization at clinically relevant concentrations. Anesthesiology *82*, 276-287; discussion 231A-232A.
Sauguet, L., Howard, R.J., Malherbe, L., Lee, U.S., Corringer, P.J., Harris, R.A., and Delarue, M. (2013a). Structural basis for potentiation by alcohols and anaesthetics in a ligand-gated ion channel. Nature communications *4*, 1697.
Sauguet, L., Poitevin, F., Murail, S., Van Renterghem, C., Moraga-Cid, G., Malherbe, L., Thompson, A.W., Koehl, P., Corringer, P.J., Baaden, M.*, et al.* (2013b). Structural basis for ion permeation mechanism in pentameric ligand-gated ion channels. EMBO J *32*, 728-741.
Sauguet, L., Shahsavar, A., Poitevin, F., Huon, C., Menny, A., Nemecz, A., Haouz, A., Changeux, J.P., Corringer, P.J., and Delarue, M. (2014). Crystal structures of a pentameric ligand-gated ion channel provide a mechanism for activation. Proceedings of the National Academy of Sciences of the United States of America *111*, 966-971.
Spurny, R., Billen, B., Howard, R.J., Brams, M., Debaveye, S., Price, K.L., Weston, D.A., Strelkov, S.V., Tytgat, J., Bertrand, S.*, et al.* (2013). Multisite binding of a general anesthetic to the prokaryotic pentameric Erwinia chrysanthemi ligand-gated ion channel (ELIC). J Biol Chem *288*, 8355-8364.
Spurny, R., Debaveye, S., Farinha, A., Veys, K., Vos, A.M., Gossas, T., Atack, J., Bertrand, S., Bertrand, D., Danielson, U.H.*, et al.* (2015). Molecular blueprint of allosteric binding sites in a homologue of the agonist-binding domain of the alpha7 nicotinic acetylcholine receptor. Proceedings of the National Academy of Sciences of the United States of America *112*, E2543-2552.
Study, R.E., and Barker, J.L. (1981). Diazepam and (--)-pentobarbital: fluctuation analysis reveals different mechanisms for potentiation of gamma-aminobutyric acid responses in cultured central neurons. Proceedings of the National Academy of Sciences of the United States of America *78*, 7180-7184.
Velisetty, P., and Chakrapani, S. (2012). Desensitization mechanism in prokaryotic ligand-gated ion channel. J Biol Chem *287*, 18467-18477.
Velisetty, P., Chalamalasetti, S.V., and Chakrapani, S. (2014). Structural basis for allosteric coupling at the membrane-protein interface in Gloeobacter violaceus ligand-gated ion channel (GLIC). J Biol Chem *289*, 3013-3025.
Weng, Y., Yang, L., Corringer, P.J., and Sonner, J.M. (2010). Anesthetic sensitivity of the Gloeobacter violaceus proton-gated ion channel. Anesth Analg *110*, 59-63.
Willenbring, D., Liu, L.T., Mowrey, D., Xu, Y., and Tang, P. (2011). Isoflurane alters the structure and dynamics of GLIC. Biophys J *101*, 1905-1912.

Winn, M.D., Ballard, C.C., Cowtan, K.D., Dodson, E.J., Emsley, P., Evans, P.R., Keegan, R.M., Krissinel, E.B., Leslie, A.G., McCoy, A.*, et al.* (2011). Overview of the CCP4 suite and current developments. Acta crystallographica. Section D, Biological crystallography *67*, 235-242.
Yip, G.M., Chen, Z.W., Edge, C.J., Smith, E.H., Dickinson, R., Hohenester, E., Townsend, R.R., Fuchs, K., Sieghart, W., Evers, A.S.*, et al.* (2013). A propofol binding site on mammalian GABAA receptors identified by photolabeling. Nat Chem Biol *9*, 715-720.
Young, G.T., Zwart, R., Walker, A.S., Sher, E., and Millar, N.S. (2008). Potentiation of alpha7 nicotinic acetylcholine receptors via an allosteric transmembrane site. Proceedings of the National Academy of Sciences of the United States of America *105*, 14686-14691.

FIGURE LEGENDS

Figure 1. (A) General architecture of a prokaryotic pentameric ligand-gated ion channel such as GLIC seen from the side (top) or from the extracellular medium (bottom). Anesthetic binding sites in the open (left) and resting (right) states are shown as colored blobs. Extracellular and transmembrane domains are highlighted in tan and cyan colors, respectively. (B) Schematic view of the main anesthetic binding sites in the TMD discussed in this manuscript seen from the side and from the top. The five sites include DP, DP' and DP-deep (Sauguet et al., 2013a), the inter-subunit DP-tunnel site predicted from simulations (Nury et al., 2011), and the new pore site presented in this work, referred to as PS. See also Table S1.

Figure 2. Locally closed GLIC structure cocrystallized with bromoform. (A) Top view of GLIC TMD with the bromine-specific anomalous map contoured at a level of 5 σ (brown mesh). (B) The pore site PS and a detergent molecule from the crystallization solution in the locally closed form of GLIC are shown as sticks. The bromine-specific anomalous map (brown mesh) and the 2mFo-DFc electron density (blue mesh) are contoured at a level of 5 σ and 1.5 σ, respectively. (C) Superimposition of the pore in the open (blue) and LC (grey) conformations. The bromoform PS binding site is located in place of ordered water molecules in GLIC's open form. (D) The intra-subunit sites DP, DP', DP-exp and DP-deep revealed in GLIC open and LC conformations. See also Figure S1.

Figure 3. Influence of Y197 sidechain orientation on its local environment. Up conformation, where Y197 does not interfere with the DP binding sites, is shown in gray. In down conformation (red color), Y197 partially overlaps the DP' subsite of DP-exp. Volumes measured for DP' in simulations are shown as boxplots for each orientation; values for crystal structures are reported as mauve triangles. See also Figure S6.

Figure 4. Bromoform exploration of the GLIC TMD in flooding simulations. Side (top) and top (bottom) views of a GLIC subunit with bromoform occupancies represented as yellow iso-surfaces. Residue Y197 is shown as sticks colored by atom type and the carbon alpha atoms of residues T244 and N245 are depicted as spheres. Unoccupied binding sites in locally-closed and closed forms are indicated by hollow circles using the site color code from Fig. 1**. See also Figure S2.**

Figure 5. Free energies of bromoform binding (kcal/mol) to six discussed binding sites. The five TMD binding site locations are depicted in the schematic above the bar chart. WT = "Wild-Type"; O = "Open"; LC = "Locally-Closed" ; C = Closed. Empirical error estimate is ±0.5 kcal/mol as discussed in the text. **See also Figure S4, S7, S8 and Table S2.**

Figure 1

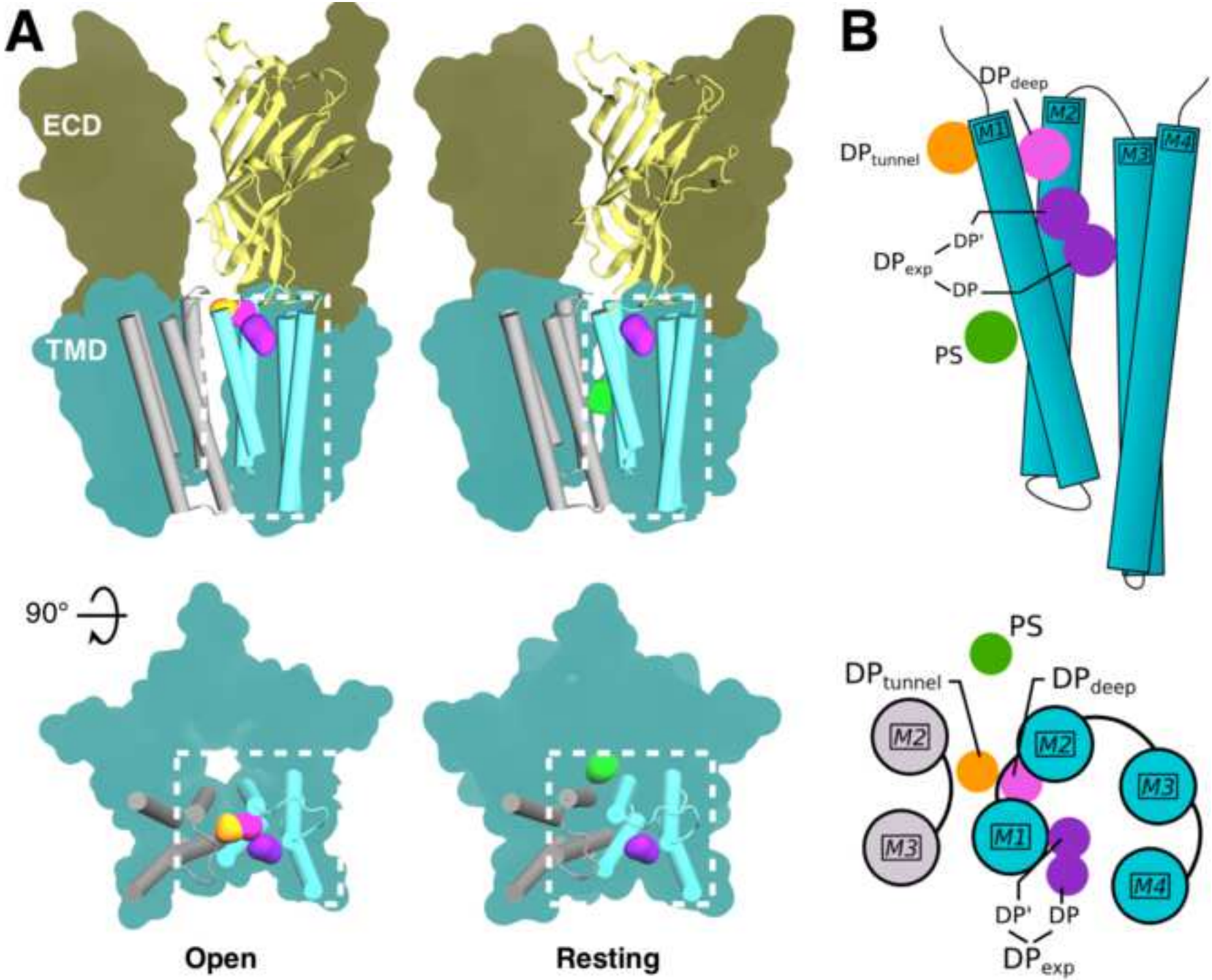
A
ECD
TMD
90°
Open
Resting
B
DP deep
DP tunnel
M1
M2
M3
M4
DP'
DP exp
DP
PS
PS
DP tunnel
DP deep
M2
M2
M3
M1
M3
M4
DP'
DP
DP exp

Figure 2

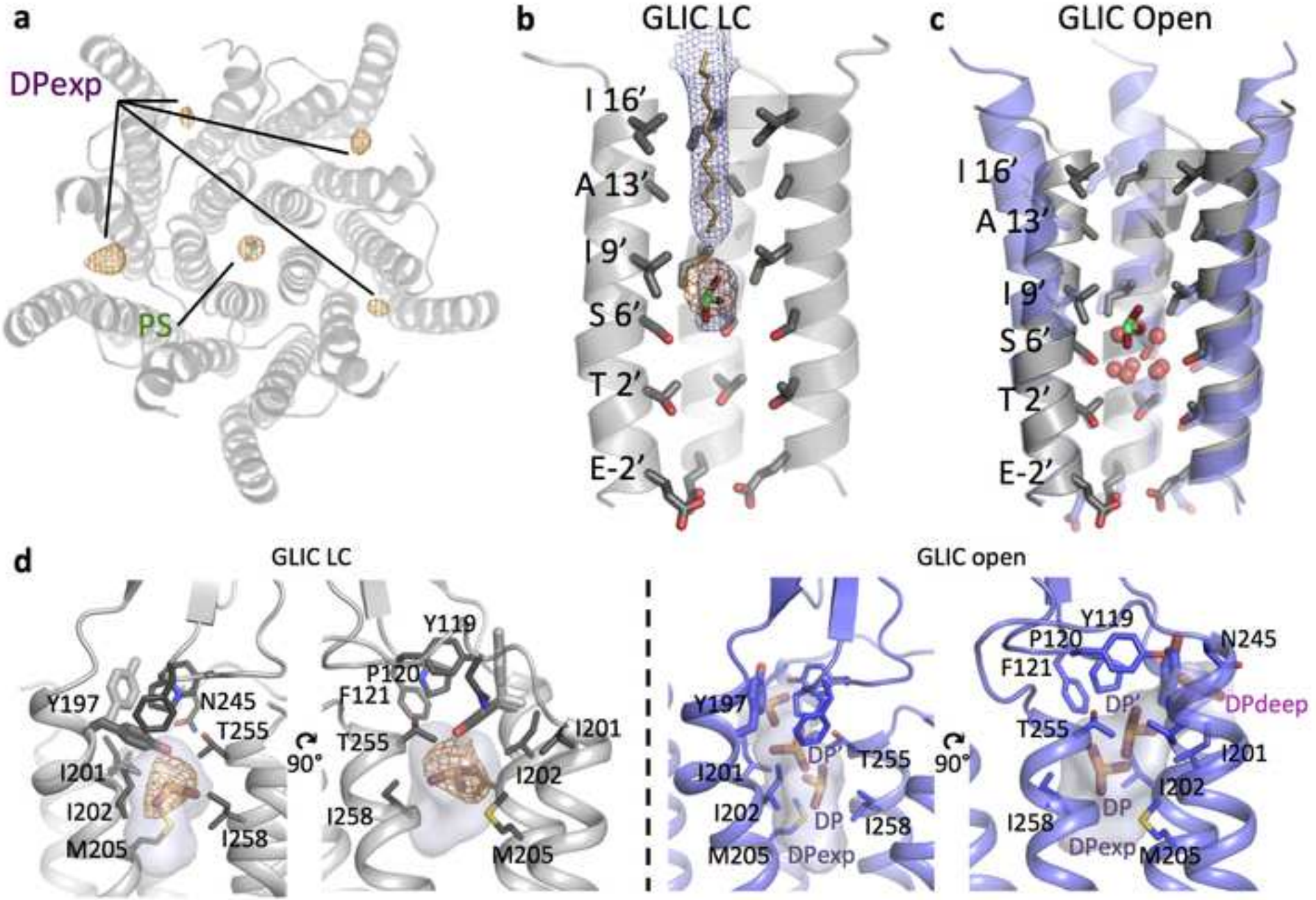
a
DPexp
PS
b
GLIC LC
I 16′
A 13′
I 9′
S 6′
T 2′
E-2′
c
GLIC Open
I 16′
A 13′
I 9′
S 6′
T 2′
E-2′
d
GLIC LC
Y197
N245
T255
I201
I202
M205
I258
90°
Y119
P120
F121
T255
I201
I202
I258
M205
GLIC open
Y197
I201
I202
M205
DP′
T255
DP
I258
DPexp
90°
Y119
P120
F121
N245
DPdeep
DP′
T255
I201
I202
DP
I258
DPexp
M205

Figure 3

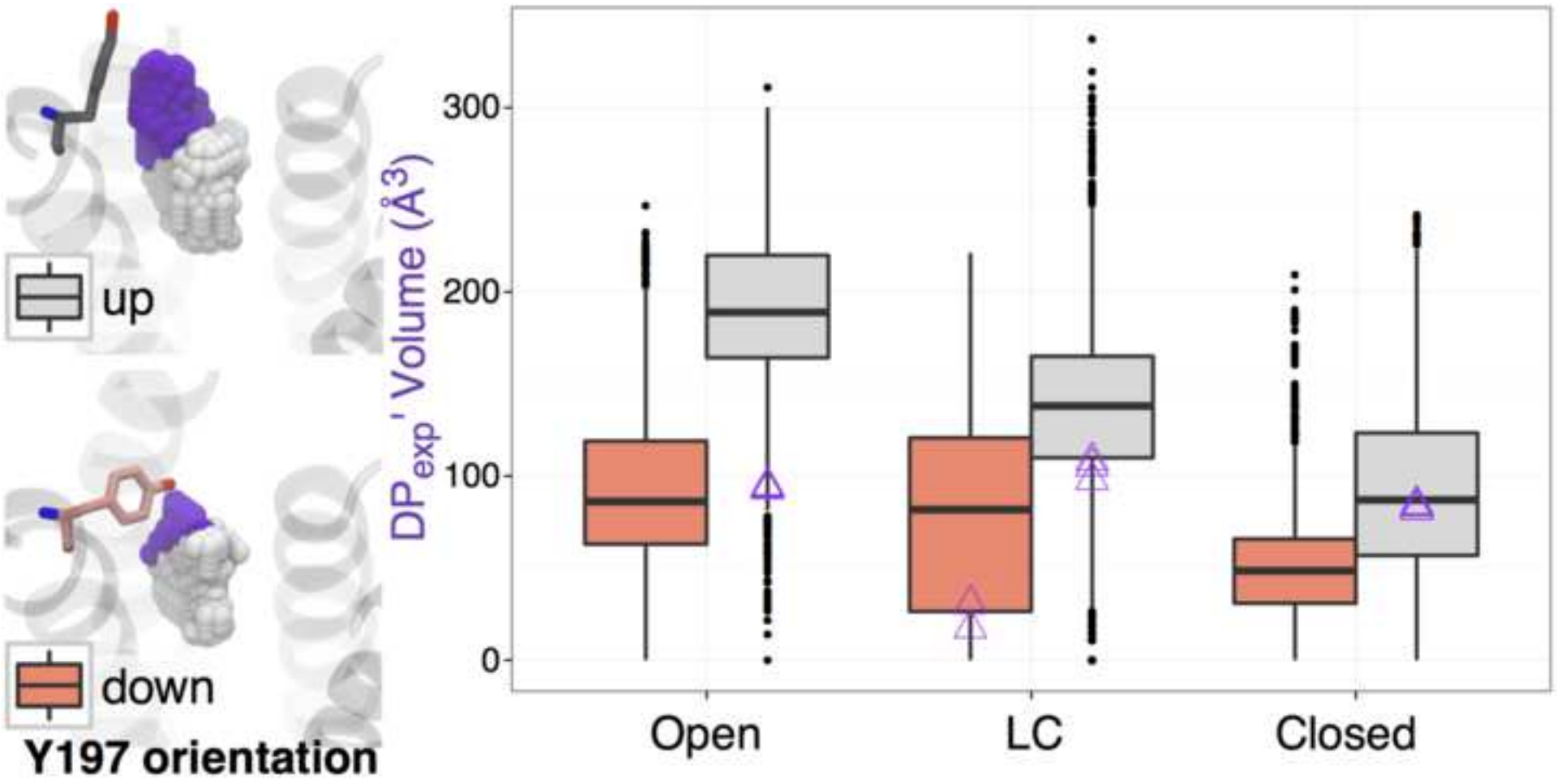
up
down
Y197 orientation
DP$_{exp}$' Volume (Å^3)
300
200
100
0
Open
LC
Closed

Figure 4

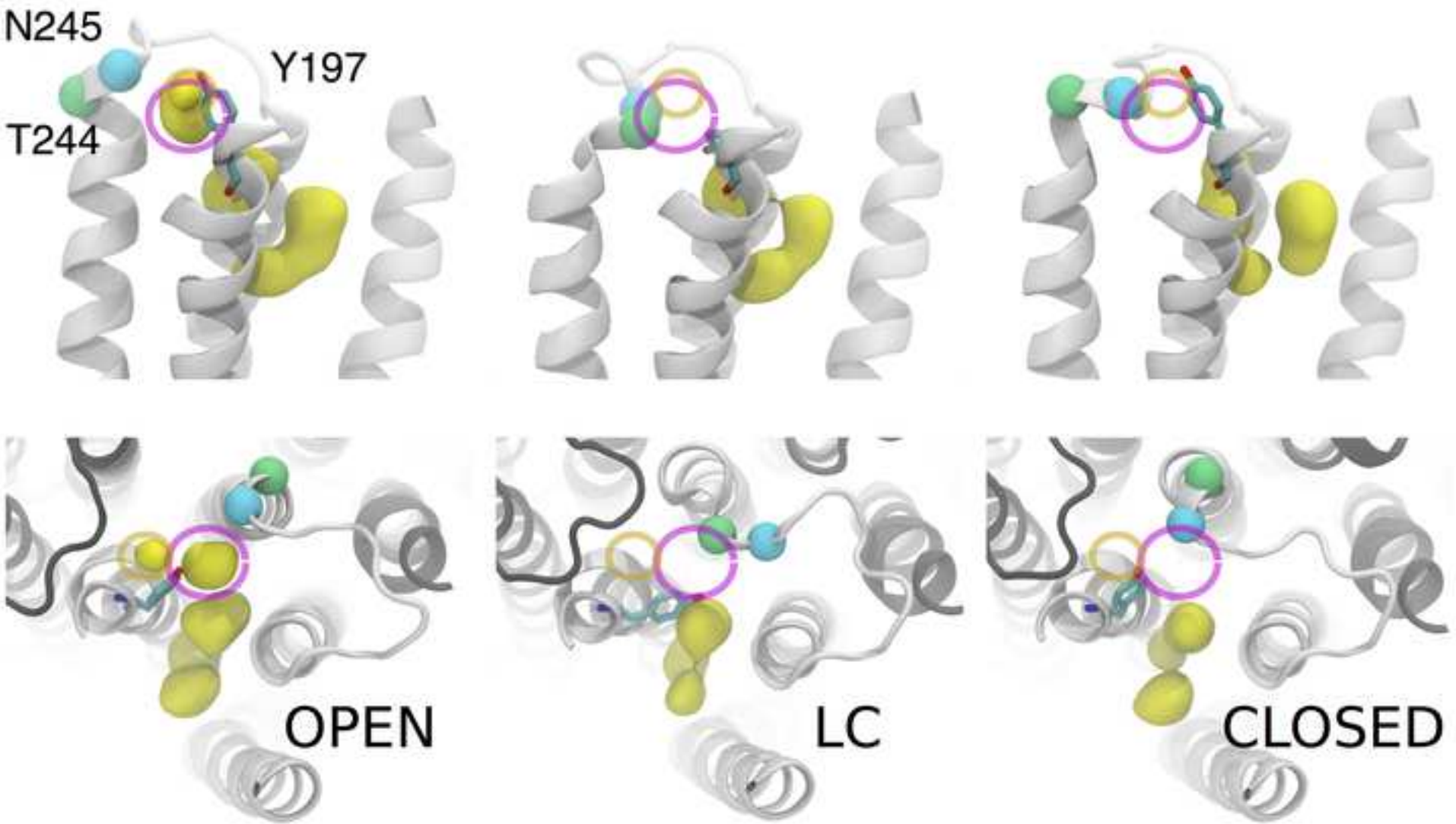

Figure 5

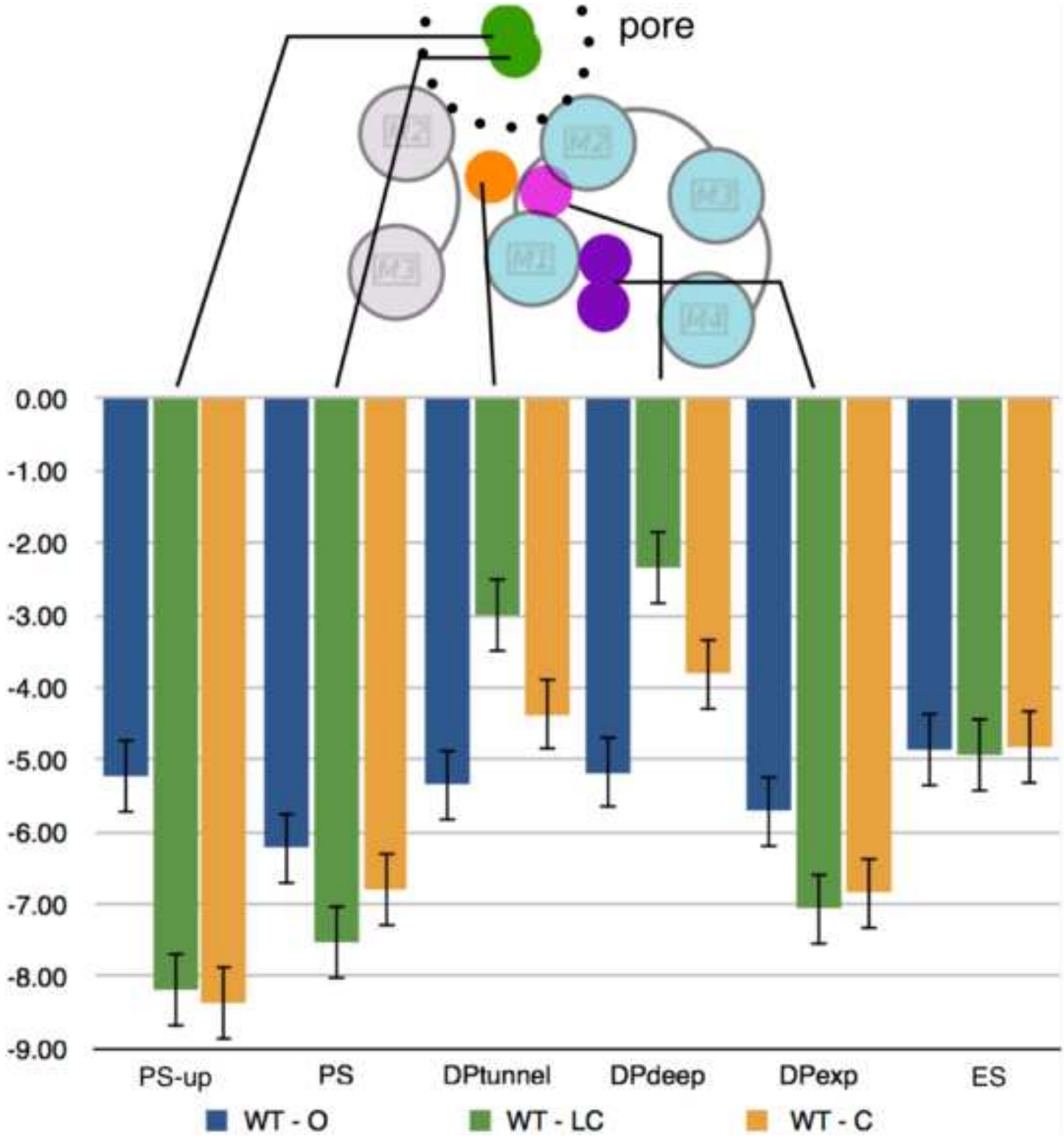
pore
0.00
-1.00
-2.00
-3.00
-4.00
-5.00
-6.00
-7.00
-8.00
-9.00
PS-up
PS
DPtunnel
DPdeep
DPexp
ES
WT - O
WT - LC
WT - C

Table 1. Data collection and refinement statistics.

	Bromoform/2-22'	Bromoform/2-21'
Data collection		
X-ray source	SOLEIL PX1	SOLEIL PX1
Wavelength (Å)	0.9184	0.9184
Space group	C2	C2
No. of monomers in the asymmetric unit	5	5
Unit cell dimensions		
Resolution range (Å)	30.0-2.95 (3.11-2.95)*	47.99-3.15 (3.32-3.15)
R_{merge}	0.051 (0.559)	0.099 (0.558)
<I/σI>	11.8 (2.1)	13.0 (2.3)
Completeness (%)	99.6 (99.7)	99.7 (98.9)
Multiplicity	3.5 (3.3)	6.6 (4.7)
No. of unique reflections	77979 (11360)	60505 (8708)
Wilson *B* (Å^2)	85.8	76.4
Refinement		
R_{work}/R_{free} (%)	21.3/21.9	23.0/24.1
No. of atoms		
Protein	12620	12600
Ligand	242	4
Average *B*-factors (Å^2)		
Root mean square deviations		
Molprobity Analysis		
Ramachandran favored (%)	94.8	97.99
Ramachandran outliers (%)	0.46	0
Molprobity score	2.23	1.50
PDB Code	5HCJ	5HCM

* Numbers in parentheses represent the last shell values.

Table 2. Systems studied by molecular dynamics simulations with corresponding sampling time.

Form	Bromoform pose	Sampling time
Long MD simulations		
Open	"Flooding"	30 ns equil. + 1μs production each
Locally-Closed		
Closed		
Short MD simulations		
Locally-Closed	PS	10 x 8 ns = 80 ns
Free energy calculations		
Open	DP-exp, DP-deep DP-tunnel, PS, PS-up, ES	32 windows sampled for 3 to 10 ns each
Locally-Closed		
Closed		

[a] **See also Table S4.**

Table 3. Site occupancy [a] in flooding simulations.

GLIC form	DP [b]	DP' [b]	DP-deep	DP-tunnel	PS
WT – O	0.57	0.44	0.36	0.12	0.50
WT – LC	0.45	0.24	0.03	0.00	0.00
WT – C	0.63	0.22	0.00	0.00	0.00

[a] Site occupancy was calculated based on a center of mass distance criterion of 4 Å with respect to crystallographic sites.

[b] Both DP and DP' sites together constitute DP_{exp}.

[c] See also Figures S3, S5, S6 and Table S3.

Sites of anesthetic inhibitory action on a cationic ligand-gated ion channel

Benoist Laurent ‡, Samuel Murail ‡, Azadeh Shahsavar §,†, Ludovic Sauguet §,&, Marc Delarue §, &, *, Marc Baaden *

Laboratoire de Biochimie Théorique, CNRS, UPR9080, Univ. Paris Diderot, Sorbonne Paris Cité, 13 rue Pierre et Marie Curie, 75005 Paris, France. § Unité de Dynamique Structurale des Macromolécules, Institut Pasteur, F-75015 Paris, France. & UMR 3258, Centre National de la Recherche Scientifique, F-75015 Paris, France.

*** Co-corresponding authors E-mail: baaden@smplinux.de; marc.delarue@pasteur.fr. † Present address: Department of Drug Design and Pharmacology, Faculty of Health and Medical Sciences, University of Copenhagen, DK-2100 Copenhagen, Denmark. ‡These authors contributed equally.**

Inventory of Supplemental Information

Supplemental Information

Supplemental Experimental Procedures

X-ray crystallography S1, related to Figure 2

Crystal preparation

All crystals were obtained using vapour diffusion in hanging drops at 20°C. The concentrated (6–8 mg/ml) protein was mixed in a 1:1 ratio with reservoir solution typically containing 16–20% PEG 2000MME, 50 mM $NiCl_2$, 4% DMSO, 11% ethylene glycol and 0.1 M NaAcetate pH 3.0. Crystallization was induced by the micro-seeding technique from a solution of crushed crystals 1 hour after setting-up the crystallization experiment. Crystals appeared overnight and grew for one week before reaching their final dimensions (typically 100 µm x 100 µm x 100 µm). All crystals were cryo-protected using a three-step protocol. 1) The crystals-containing drops were transferred to the cold room (4°C), sealed onto a novel crystal plate that contained no reservoir solution and left at 4°C for 10 minutes. 2) 3-5 µl of a dehydrating solution composed of the reservoir solution supplemented with 30% of ethylene glycol was added to the crystallization drop. 3) The drop was left to air-dry for 5-20 minutes prior to flash-freezing in liquid nitrogen.

Data collection

Datasets were collected on beamline Proxima-1 of the Soleil Synchrotron (Gif-sur-Yvette, France). Crystals were collected using the inversed-beam data collection facility in order to maximize the anomalous diffusion signal. Reflections were integrated using XDS (1) and further processed using the CCP4 programs (2). Crystals belonged to the C2 space group with one pentamer in the asymmetric unit. Details on the data collection statistics are provided in the Table 1.

Phasing and refinement

The molecular replacement solution was found in Phaser (3) by using the structure of GLIC K33C L246C double-mutant (PDB 3UU6) at 2.9 Å as a starting model. This initial model was refined in Refmac 5 (4) by using rigid-body refinement and subsequently, by using restrained refinement (4). The resulting model was improved by manual building in COOT (5). The model was finally refined in Buster (6). B-factors were refined using 1 TLS parameter by chain. NCS symmetry averaging improves the quality of the electron density thus allowing the unambiguous reconstruction of the model. Rfactor and Rfree after refinement as well as model geometry validation percentile of the residues in the most favoured regions of the Ramachandran plot are provided in Table 1. MolProbity scores (7) for the refined model ranged within the 100^{th} percentiles of structures refined at comparable resolutions. Details of the refinement statistics are provided in Table 1.

Supplemental Computational Methods

Molecular dynamics simulations S1, related to Table 2

Molecular models of open GLIC were built from PDB ID 4HFI. Residue protonation states of open and LC models were assigned in the same fashion as in previous simulations (8) on the basis of pKa calculations with the Yasara software (9) to represent the most probable pattern at pH 4.6, with residues E26, E35, E67, E69, E75, E82, D86, D88, E177 and E243 being protonated. All histidines were doubly protonated (unless advised). The molecular model of GLIC in the resting state was built from PDB ID 4NPQ, protonation state was chosen to be identical to the resting condition at neutral pH, glutamic acid and aspartic acid residues were unprotonated and only histidine 127 was doubly protonated. The models were inserted in a fully hydrated palmitoyl-2-oleoyl-sn-glycerol-phosphatidylcholine (POPC) lipid bilayer. The net charge of the system was neutralized with Na^+ and Cl^- counter ions. Details are given in Supplementary Table 4.
MD simulations were performed using the CHARMM27 (10) force field with NAMD (11) and CHARMM 36 (12) with GROMACS (13) for short and long MD simulations, respectively.

For short MD simulations, bromoform was inserted into a previously equilibrated system of GLIC embedded in a fully hydrated lipid bilayer. Bromoform poses were generated by randomly moving and

rotating bromoform molecules around the crystallographic binding site. Bromoform molecules were assigned different conformations in each of the five GLIC subunits and in each of the 25 systems that were simulated achieving a total of 125 different poses, which maximizes bromoform sampling in the binding pocket. Each system was then minimized for 1000 steps and ran for 8 ns. Temperature and pressure were maintained using Langevin dynamics (14) and a Langevin Piston (15), respectively, at 310 K and 1 bar. Short-range non-bonded interactions were computed using a potential switching from 8.5 to 10 Å. Long-range interactions have been carried out using PME (16). The same protocol has been used for the simulation of bromoform bound to WT locally closed GLIC in PS site.

For long MD simulations a previously equilibrated system containing GLIC, 246 POPC, 29141 water, 170 Cl^- and 135 Na^+ molecules (146 K atoms) in an hexagonal box was used to create the system with 200 bromoform molecules. It was equilibrated for 50 ns with position constraints on GLIC C_α atoms with 4HFI structure as a reference. Then four iterations were used to add slowly the bromoform and avoid aggregates due to its low solubility. In each iteration, 50 molecules of bromoform were added by replacing random water molecules 10 Å away of protein and 4 Å away of the membrane. The system was then minimized for 10.000 steps and equilibrated with position constraints on GLIC C_α atoms with 4HFI structure as a reference. In the two first iterations, equilibrations were 50 ns long, and 100 ns long in the two following. In a last step bromoform molecules which were bound in the intra-subunit cavity were replace in the water and system was minimized for 10.000 steps.
This equilibrated system was then used as starting point for the three flooding simulations. In each of the three simulations, a supplementary equilibration step was used consisting in a 10 ns equilibration with position constraints on heavy atoms, and 20 ns with position constraints on C_α atoms. Reference structures used were, for WT Open and WT LC simulations, respectively, PDB:4HFI, the structure presented in this paper and PDB:4HFD. Production runs were finally run for 1 µs without any constraints.
Simulations were performed using GROMACS 4.6.3 (13) using virtual interaction sites, 5 fs time steps, and all bond lengths constrained with the LINCS algorithm. Electrostatics interactions were computed using particle mesh ewald summation every step. A 10 Å cutoff was used for non-bonded interactions and neighbor list was updated every 5 steps. Three baths (protein, water and ion, membrane) were coupled to a temperature of 310 K using the Bussi velocity rescaling thermostat with a time constant of τ= 0.1 ps. The x/y dimensions were scaled isotropically with a Berendsen weak barostat and the z dimension independently to reference pressures of 1 bar, τ = 5 ps and compressibility of 4.5 10^{-5} bar^{-1}. During equilibration position restraints of 1000 kJ/mol/nm^2 were used.

For free energy of binding energy calculations, the bromoform poses displayed in the crystal structure were used when available. The bromoform pose in inter-subunit site B2 was extracted from a short MD simulation. Bromoform was inserted into a previously equilibrated system of GLIC embedded in a fully hydrated lipid bilayer. The system was then minimized for 10,000 steps. Two successive equilibrations with constraints on a reference structure, typically a crystal structure, were performed: 5 ns constraining protein heavy atoms and bromoform then 20 ns constraining protein carbon alpha atoms and bromoform. During these two equilibration steps, constraints were also applied on the dihedral angle between Y197 C-CA-CB-CG atoms ensuring an angle of 173.5 ° in GLIC open form and 91.8 ° in the locally closed conformation. These values correspond to the two principal modes of the angle distribution observed along short MD simulations. A thermodynamic cycle was then applied to calculate free energies of binding of bromoform to GLIC using a similar protocol as that described in (17). Coulombic and van der Waals interactions were decoupled using a decoupling parameter λ linearly increasing from 0 to 1. Coulombic interactions were decoupled along 11 independent steps while 21 steps were necessary to decouple van der Waals interactions. At each λ-point, the system was minimized for 5000 steps, equilibrated for 10 ps in the NVT ensemble then equilibrated for 100 ps in the NPT ensemble. The bromoform position was constrained during these two equilibration steps. Production simulations were run using the sd integrator with a time step of 2 fs. For coulombic interaction decoupling, 2 ns were carried out. For van der Waals interactions, 3 ns were carried out for the first 14 λ-points (initial $\lambda < 0.7$) and 10 ns for the remaining 7 points (initial $\lambda >= 0.7$). The same protocol was applied for decoupling bromoform in water. The calculation of the binding free energy was carried out using the Bennett acceptance ratio method (BAR) (18) as implemented in the GROMACS g_bar program.

PMF calculation. A small membrane patch was extracted from an equilibrated system of GLIC in a POPC membrane. The patch contains 72 POPC molecules, 5549 water molecules, and 29 Cl- and Na+ atoms. The current membrane patch was minimized and equilibrated for 50 ns. A bromoform molecule was then introduced 35 Å up the center of mass of the membrane, 5 overlapping water molecules were deleted. After minimization, the bromoform was pulled down on the z axis, relative to the center of mass of the membrane, using the constraint method from the Gromacs pull code. The bromoform molecule was free to move on the x/y plane, and was pulled with a rate of 7 Å/ns, during 10ns, resulting in a 70 Å displacement on the z axis.
Coordinates were extracted regularly every ~285 ps from the pull trajectory, resulting in 36 coordinates in which the bromoform was distributed every 2 Å on the 70 Å total displacement on the z-axis. 36 umbrella sampling simulations were launched for 20 ns each, bromoform distance to the membrane on the z-axis was restraint with harmonic restraints of 1000 KJ.nm-1. The g_wham tool from gromacs was then used on the last half of the 36 simulations, the profile was symmetrized around z = 0 Å. Statistical errors were estimated with the boostrap method using 200 samples.

Bromoform likelyhood from flooding simulations. Bromoform z positions respective to the membrane were extracted from the three flooding simulations (Open, LC, Closed). Bromofrom molecules too close to the protein were excluded from the calculation, using a 40 Å exclusion cylinder from the center of mass of the trans membrane domain of GLIC. We used Boltzmann weighting (-kT log(p)) to obtain the probability profile shown in Figure S8.

Supplemental Figures

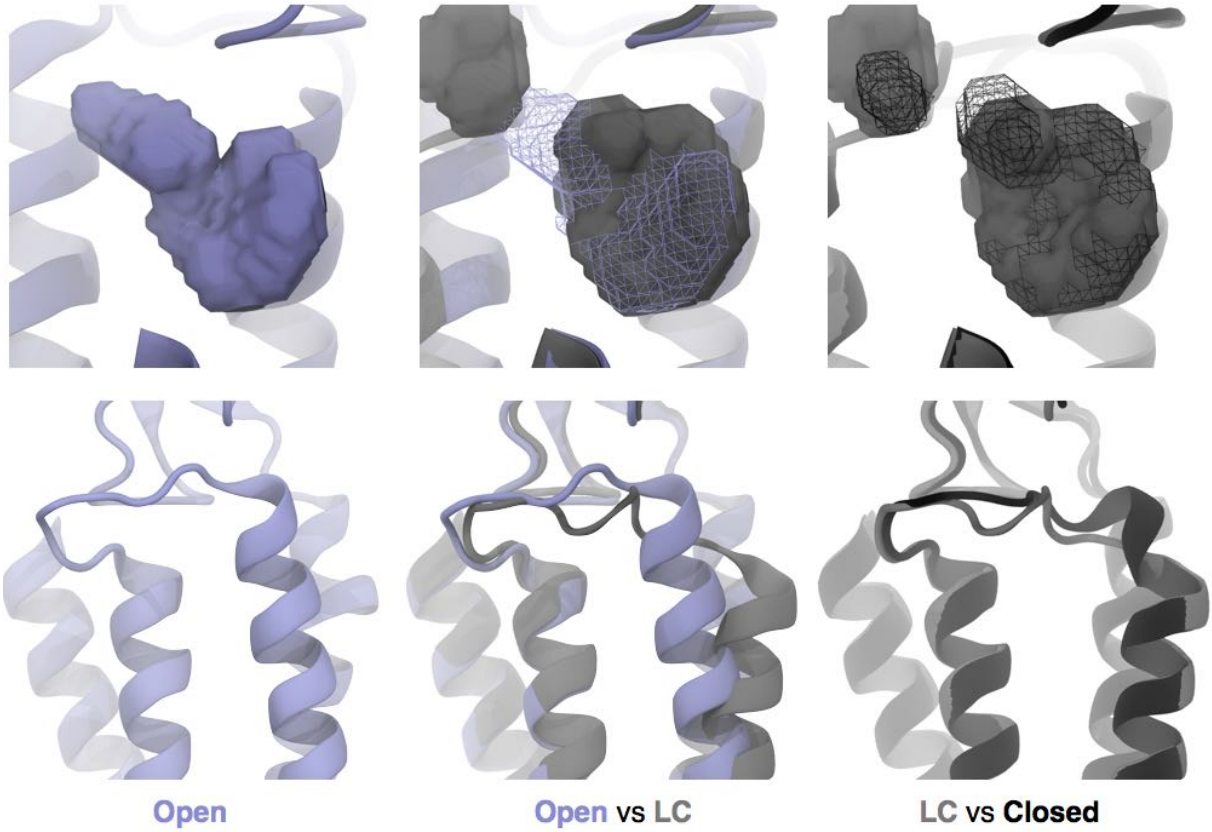

Figure S1, related to Figure 1. Comparison of transmembrane anesthetic binding cavities (top row) and transmembrane subunit conformations (bottom row) for open, locally-closed (LC) and closed channel conformations (PDB IDs 4HFH, 5HCJ and 4NPQ, respectively colored in purple, gray and black). Anesthetic binding cavities were determined with the Epock software (19).

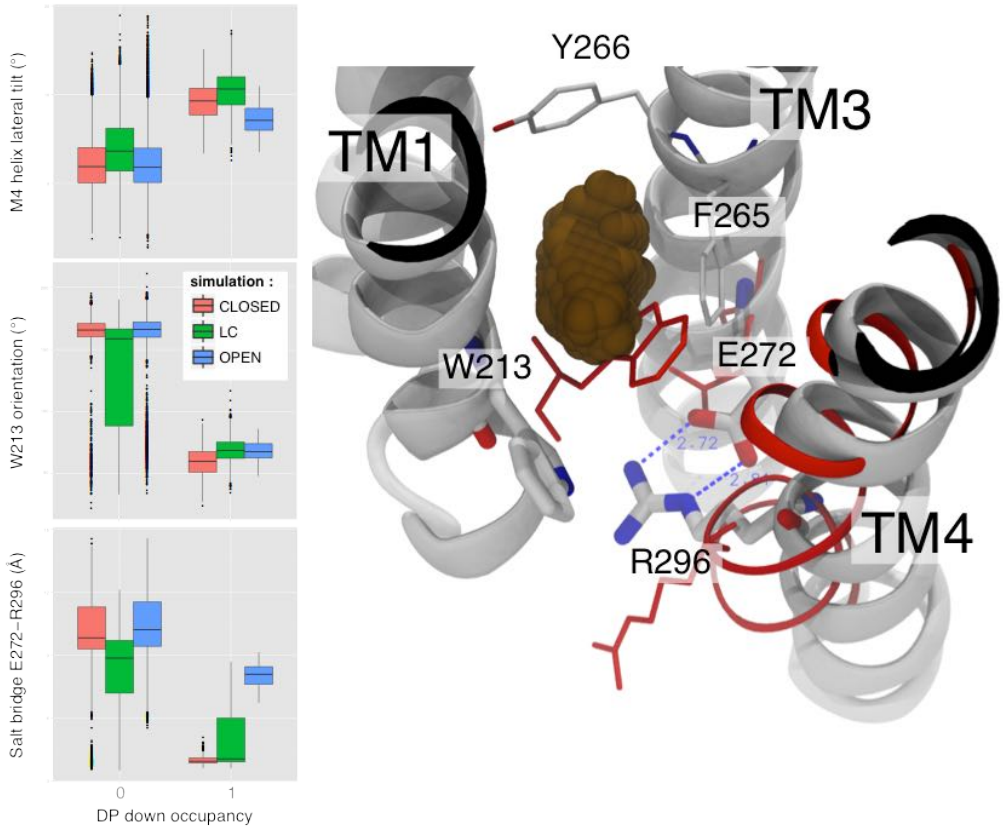

Figure S2, related to Figure 4. The right panel shows a structural view of the bromoform site TM-down (brown spheres) in the lower part of the intra-subunit TMD helical bundle surrounded by residues L209, S212 and W213 on M1 and residues F265, Y266 on M3. Important features such as the R296-E272 salt bridge and the conformation of several aromatic residues that control this site are highlighted. The three panels on the left correlate the occupancy of the TM-down site with the M4 helix lateral tilt, the W213 orientation and the existence of the E272-R296 salt bridge.

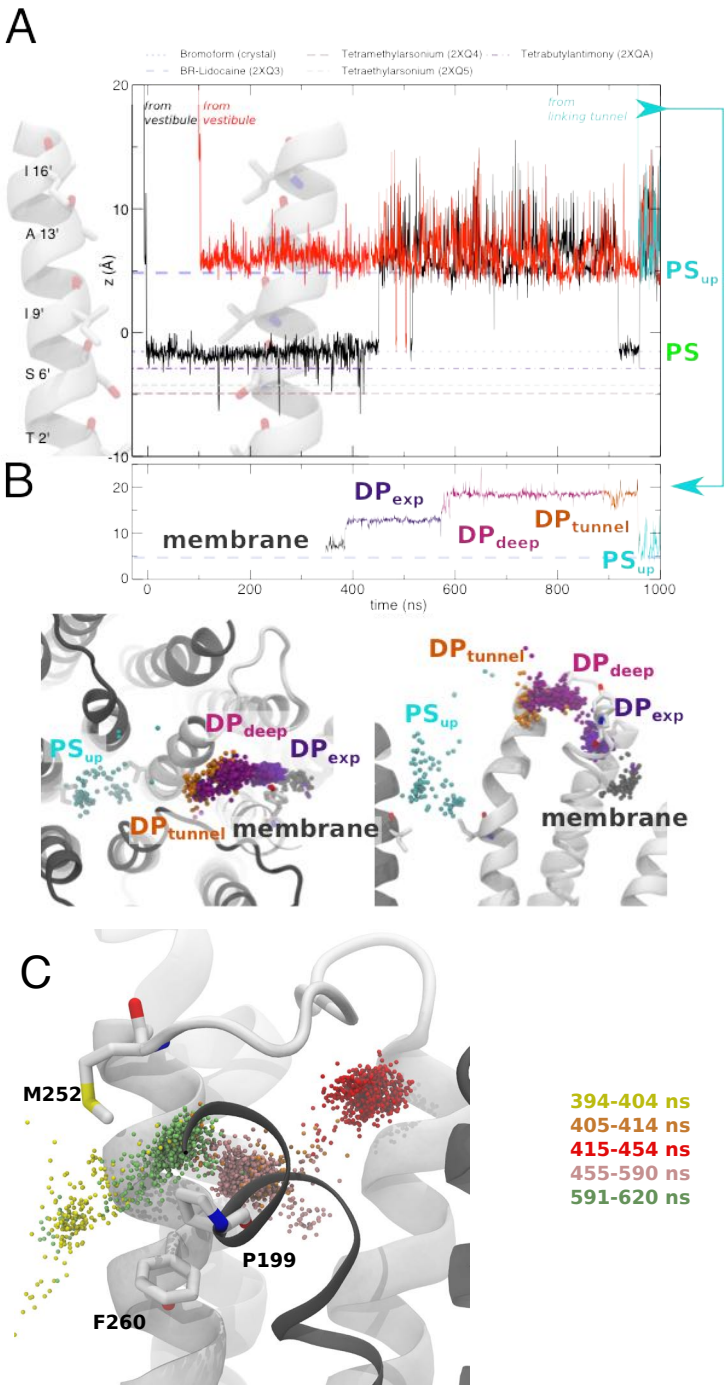

Figure S3, related to Table 3. Bromoform access to the pore and TMD. **A)** Time series of z positions perpendicular to the membrane plane for three bromoform molecules entering the pore region in the WT-O flooding simulation, z position measured with respect to the TMD center of mass. Two anaesthetic molecules coming from the channel vestibule reach the pore site PS (dotted blue line) slightly above the S6' position. All bromoform molecules visit an upper pore site PS-up (dashed blue line) between I9' and A13'. Other experimentally observed pore binding sites are indicated by additional lines. **B)** Transition of the third bromoform molecule entering the pore. This molecule travels from the membrane to the PS-up site. Time series of z positions perpendicular to the membrane plane (top), top (bottom left) and side (bottom right) views of a GLIC subunit with bromoform location indicated as colored spheres every 0.5 ns. Over ~570 ns, this bromoform molecule passes from the membrane to site DP-exp, DP-deep, DP-tunnel and ultimately the pore. **C)** Direct entry and exit of a bromoform molecule into site DP-tunnel in the resting form flooding simulation. The anesthetic originates directly from the membrane (yellow) and passes through TM helices (orange) into DP-tunnel (red) where it stays for a brief period before exiting again (pink, followed by green).

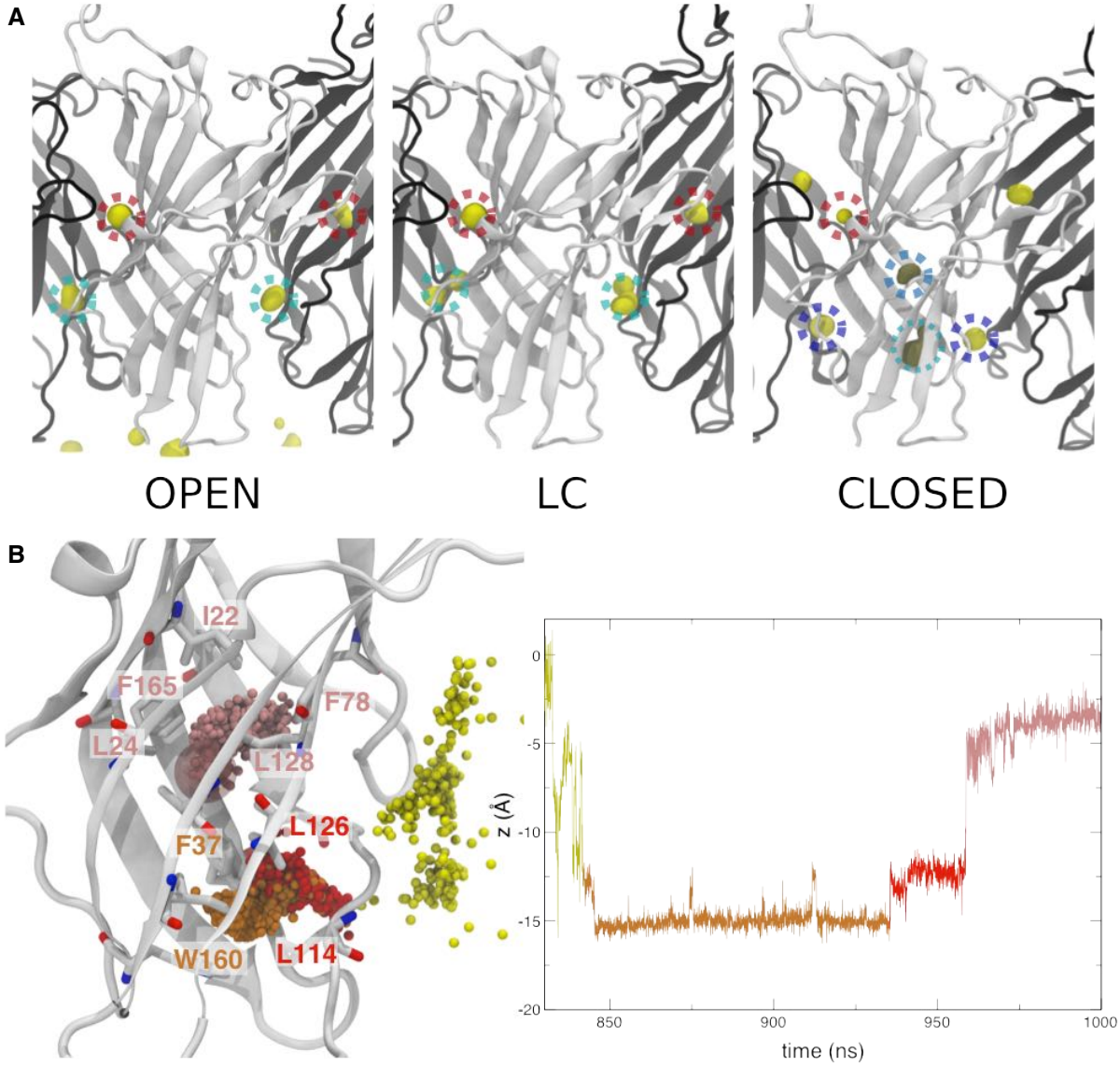

Figure S4, related to Figure 5. A) Bromoform density isosurfaces (yellow) in the ECD for open, LC and closed states. Equivalent sites among states are encircled by the same color. Sites indicated by red circles are well occupied in open and LC form but weakened in the closed one. The sites marked by cyan circles exist in open and LC form, yet vanish in the closed form, where a new site marked in dark blue appears. The ES-access and ES sites (light- and mid-blue coloring, respectively) only exist at the end of the closed state simulation in one subunit and are shown for comparison, but not to scale. **B)** Bromoform entering an ECD cavity through the ES-access site in the resting state. The left panel shows transitions of one bromoform molecule with its carbon atom represented as small spheres at 0.05 ns interval colored according to the time window in the simulation. The ES site position observed at the end of the simulation is very close to a bromoform molecule crystallized in the ELIC ECD, shown as transparent sphere. The right panel features the time series of bromoform z positions perpendicular to the membrane plane measured with respect to the ECD center of mass.

Figure S5, related to Table 3. The top panel schematically illustrates the transitions between TMD sites observed in the flooding simulations of open, locally-closed and closed states. Each site is depicted as a circle, the size being proportional to site occupancy, also indicated as percentage. Arrows schematize transitions and their count is indicated next to the arrow. The bottom panels indicate the distribution of residence times for each site (same color code) with a focus on long residence times. The inset provides the full curve scaled to show the maximal count of short residence times.

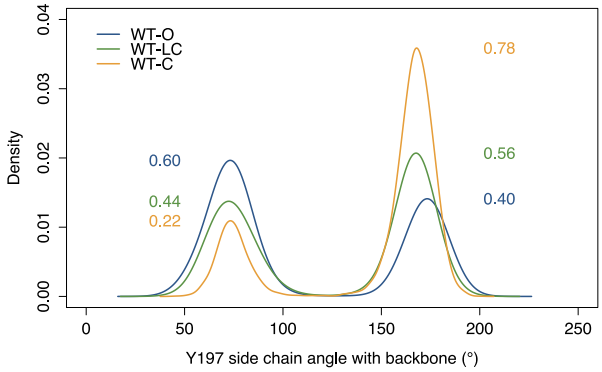

Figure S6, related to Figure 3. Distribution of the Y197 side chain orientation along flooding MD simulations for each simulation system, namely wild-type (WT) open (O), locally closed (LC) and closed (C) conformations. Note that the number of transitions from one conformation to another in the whole simulation set is low (i.e. ranges from 0 to 31 with an average of 11 ± 10 transitions per microsecond and per subunit) which prohibits correlation between Y197 side chain conformation and channel state. Densities have been calculated over a microsecond period with a time step of 0.5 ns, leading to a total of 10,000 points per density (2000 x 5 subunits).

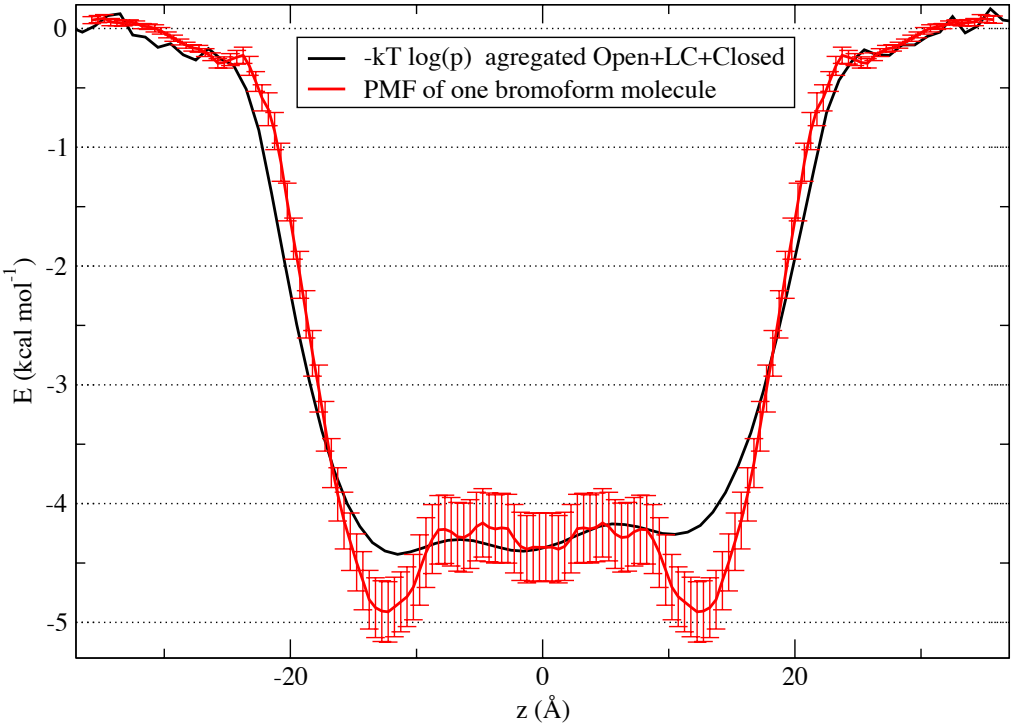

Figure S7, related to Figure 5. Free energy profiles of bromoform molecules across a POPC membrane, comparison of the PMF of a single bromoform molecule across a POPC membrane *vs.* energy profile extracted from the three flooding simulations (Open, LC, Closed). The PMF profile was estimated by symmetrizing around z=0.

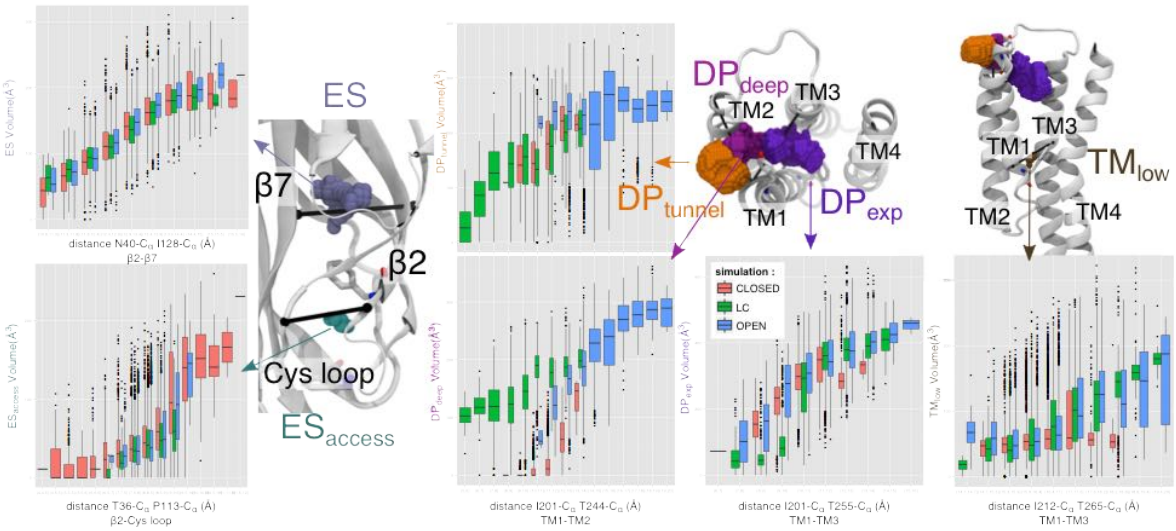

Figure S8, related to Figure 5. The volume for each of the ES, ES-access, DP-tunnel, DP-deep, DP-exp and TM-low sites was measured for all flooding simulations using the Epock software and correlated to structural changes described by characteristic distances across the channel architecture. The ES site volume correlates with the beta2-beta7 widening. The ES-access site volume is dependent on the distance between beta2 and cys-loop. DP-tunnel and DP-deep are most affected by TM1-TM2 separation. DP-exp and TM-low are sensitive to TM1-TM3 distances.

Supplemental Tables

Table S1, related to Figure 1. Crystal structures of general anaesthetics bound to GLIC (and ELIC).

PDB ID	Channel and state	Ligand	Resolution (Å)	Binding site	Reference
3P50	GLIC – O	Propofol	3.30	DP	(8)
3P4W	GLIC – O	Desflurane	3.10	DP	(8)
4HFH	GLIC – O	Bromoform	2.65	DP, DP', DP-deep	(20)
3ZKR	ELIC – C*	Bromoform	3.65	PS-up	(21)

* An additional inter-subunit (IS) site was described in this structure.

Table S2, related to Figure 5. Bromoform free energy of binding in kcal/mol.

Binding site	WT-O	WT-LC	WT-C
DP-exp	**-5.7**	**-7.1**	-6.8
DP-deep	**-5.2**	-2.3	-3.7
DP-tunnel	-5.4	-3.0	-4.3
PS	-5.8	**-7.5**	-6.4
PS-up	-5.2	-8.2	-8.4
ES	-4.9	-4.9	-4.8

* WT = "Wild-Type"; O = "Open"; LC = "Locally-Closed"; C="Closed". Experimentally observed site energies are highlighted in boldface.

Table S3, related to Table 3. Bromoform occupancy of intrasubunit sites along flooding MD simulations according to the Y197 residue side chain orientation.

Y197 orientation	GLIC subtype*	DP	DP'	DP-deep
Up	WT – O	0.16	0.28	0.32
	WT – LC	0.29	0.20	0.03
	WT – C	0.48	0.21	0.00
Down	WT – O	0.41	0.16	0.04
	WT – LC	0.16	0.04	0.00
	WT – C	0.15	0.01	0.00

* WT = "Wild-Type"; O = "Open"; LC = "Locally-Closed"; C="Closed".

Table S4, related to Table 2. MD simulation system composition.

	Free energy calculations	Short MD simulations	Flooding simulations at pH 4.6	Flooding simulations at pH 7.0
Water	29,141	43,882	28,934	28,934
Lipid	246	307	246	246
Na^+	135	54	135	135
Cl^-	170	89	170	110
Salt	~300 mM	~100 mM	~300 mM	~230 mM

References

1. Kabsch W (2010) Integration, scaling, space-group assignment and post-refinement. *Acta Cryst.* D66:133-144.
2. Anonymous (1994) The CCP4 suite: programs for protein crystallography. *Acta Crystallogr D Biol Crystallogr* 50(Pt 5):760-763.
3. McCoy AJ*, et al.* (2007) Phaser crystallographic software. *J Appl Crystallogr* 40(Pt 4):658-674.
4. Murshudov GN, Vagin AA, & Dodson EJ (1997) Refinement of macromolecular structures by the maximum-likelihood method. *Acta crystallographica. Section D, Biological crystallography* 53(Pt 3):240-255.
5. Emsley P & Cowtan K (2004) Coot: model-building tools for molecular graphics. *Acta crystallographica. Section D, Biological crystallography* 60(Pt 12 Pt 1):2126-2132.
6. Blanc E*, et al.* (2004) Refinement of severely incomplete structures with maximum likelihood in BUSTER-TNT. *Acta crystallographica. Section D, Biological crystallography* 60(Pt 12 Pt 1):2210-2221.
7. Davis IW*, et al.* (2007) MolProbity: all-atom contacts and structure validation for proteins and nucleic acids. *Nucleic Acids Res* 35(Web Server issue):W375-383.
8. Nury H*, et al.* (2011) X-ray structures of general anaesthetics bound to a pentameric ligand-gated ion channel. *Nature* 469(7330):428-431.
9. Krieger E, Dunbrack RL, Jr., Hooft RW, & Krieger B (2012) Assignment of protonation states in proteins and ligands: combining pKa prediction with hydrogen bonding network optimization. *Methods Mol Biol* 819:405-421.
10. MacKerell AD*, et al.* (1998) All-atom empirical potential for molecular modeling and dynamics studies of proteins. *The journal of physical chemistry. B* 102(18):3586-3616.
11. Phillips JC*, et al.* (2005) Scalable molecular dynamics with NAMD. *J Comput Chem* 26(16):1781-1802.
12. Klauda JB, Monje V, Kim T, & Im W (2012) Improving the CHARMM force field for polyunsaturated fatty acid chains. *The journal of physical chemistry. B* 116(31):9424-9431.
13. Pronk S*, et al.* (2013) GROMACS 4.5: a high-throughput and highly parallel open source molecular simulation toolkit. *Bioinformatics* 29(7):845-854.
14. Kubo R, Toda M, & Hashitsume N (1992) *Statistical Physics II - Nonequilibrium Statistical Mechanics* (Springer New York).
15. Feller SE, Zhang Y, Pastor RW, & Brooks BR (1995) Constant pressure molecular dynamics simulation: The Langevin piston method. *The Journal of Chemical Physics* 103(11):4613.
16. Darden T, York D, & Pedersen L (1993) Particle mesh Ewald: An N·log(N) method for Ewald sums in large systems. *The Journal of Chemical Physics* 98(12):10089.
17. Bromstrup T, Howard RJ, Trudell JR, Harris RA, & Lindahl E (2013) Inhibition versus potentiation of ligand-gated ion channels can be altered by a single mutation that moves ligands between intra- and intersubunit sites. *Structure* 21(8):1307-1316.
18. Bennett CH (1976) Efficient estimation of free energy differences from Monte Carlo data. *Journal of Computational Physics* 22(2):245-268.
19. Laurent B*, et al.* (2015) Epock: rapid analysis of protein pocket dynamics. *Bioinformatics* 31(9):1478-1480.
20. Sauguet L*, et al.* (2013) Structural basis for potentiation by alcohols and anaesthetics in a ligand-gated ion channel. *Nature communications* 4:1697.
21. Spurny R*, et al.* (2013) Multisite binding of a general anesthetic to the prokaryotic pentameric Erwinia chrysanthemi ligand-gated ion channel (ELIC). *J Biol Chem* 288(12):8355-8364.